


RESEARCH

Open Access



# Thrombopoietin mimetic stimulates bone marrow vascular and stromal niches to mitigate acute radiation syndrome

Justin Vercellino<sup>1,2</sup>, Beata Małachowska<sup>1</sup>, Shilpa Kulkarni<sup>1,8</sup>, Brett I. Bell<sup>1,2</sup>, Shahin Shajahan<sup>1</sup>, Kosaku Shinoda<sup>3</sup>, Gary Eichenbaum<sup>4,9</sup>, Amit K. Verma<sup>5</sup>, Sanchita P. Ghosh<sup>6</sup>, Weng-Lang Yang<sup>1</sup>, Paul S. Frenette<sup>7^</sup> and Chandan Guha<sup>1,2,9\*</sup> 

## Abstract

**Background** Acute radiation syndrome (ARS) manifests after exposure to high doses of radiation in the instances of radiologic accidents or incidents. Facilitating regeneration of the bone marrow (BM), namely the hematopoietic stem and progenitor cells (HSPCs), is key in mitigating ARS and multi-organ failure. JNJ-26366821, a PEGylated thrombopoietin mimetic (TPOm) peptide, has been shown as an effective medical countermeasure (MCM) to treat hematopoietic-ARS (H-ARS) in mice. However, the activity of TPOm on regulating BM vascular and stromal niches to support HSPC regeneration has yet to be elucidated.

**Methods** C57BL/6J mice (9–14 weeks old) received sublethal or lethal total body irradiation (TBI), a model for H-ARS, by <sup>137</sup>Cs or X-rays. At 24 h post-irradiation, mice were subcutaneously injected with a single dose of TPOm (0.3 mg/kg or 1.0 mg/kg) or PBS (vehicle). At homeostasis and on days 4, 7, 10, 14, 18, and 21 post-TBI with and without TPOm treatment, BM was harvested for histology, BM flow cytometry of HSPCs, endothelial (EC) and mesenchymal stromal cells (MSC), and whole-mount confocal microscopy. For survival, irradiated mice were monitored and weighed for 30 days. Lastly, BM triple negative cells (TNC; CD45<sup>-</sup>, TER-119<sup>-</sup>, CD31<sup>-</sup>) were sorted for single-cell RNA-sequencing to examine transcriptomics after TBI with or without TPOm treatment.

**Results** At homeostasis, TPOm expanded the number of circulating platelets and HSPCs, ECs, and MSCs in the BM. Following sublethal TBI, TPOm improved BM architecture and promoted recovery of HSPCs, ECs, and MSCs. Furthermore, TPOm elevated VEGF-C levels in normal and irradiated mice. Following lethal irradiation, mice improved body weight recovery and 30-day survival when treated with TPOm after <sup>137</sup>Cs and X-ray exposure. Additionally, TPOm reduced vascular dilation and permeability. Finally, single-cell RNA-seq analysis indicated that TPOm increased the expression of collagens in MSCs to enhance their interaction with other progenitors in BM and upregulated the regeneration pathway in MSCs.

We dedicate this paper to the memory of Dr. Paul S. Frenette.

<sup>^</sup>Deceased: Paul S. Frenette.

\*Correspondence:

Chandan Guha  
cguhamd@gmail.com

Full list of author information is available at the end of the article



© The Author(s) 2024. **Open Access** This article is licensed under a Creative Commons Attribution 4.0 International License, which permits use, sharing, adaptation, distribution and reproduction in any medium or format, as long as you give appropriate credit to the original author(s) and the source, provide a link to the Creative Commons licence, and indicate if changes were made. The images or other third party material in this article are included in the article's Creative Commons licence, unless indicated otherwise in a credit line to the material. If material is not included in the article's Creative Commons licence and your intended use is not permitted by statutory regulation or exceeds the permitted use, you will need to obtain permission directly from the copyright holder. To view a copy of this licence, visit <http://creativecommons.org/licenses/by/4.0/>. The Creative Commons Public Domain Dedication waiver (<http://creativecommons.org/publicdomain/zero/1.0/>) applies to the data made available in this article, unless otherwise stated in a credit line to the data.

**Conclusions** TPOm interacts with BM vascular and stromal niches to locally support hematopoietic reconstitution and systemically improve survival in mice after TBI. Therefore, this work warrants the development of TPOm as a potent radiation MCM for the treatment of ARS.

**Keywords** Hematopoietic acute radiation syndrome, Total body irradiation, Bone marrow, Mesenchymal stromal cells, Endothelial cells, Thrombopoietin mimetic

## Background

Exposure to ionizing radiation, whether from accidental incidents or as a preparative regimen for allogeneic stem cell transplantation to treat leukemias, results in profound bone marrow (BM) injury. Total body irradiation (TBI) can affect various organ systems, with the hematopoietic system being the most radiosensitive [1, 2]. Preserving and reconstituting hematopoietic stem and progenitor cells (HSPCs) in the BM is crucial for mitigating mortality from hematopoietic acute radiation syndrome (H-ARS), typically occurring after high-dose TBI over a short period of time [3, 4]. HSPCs comprise all blood and immune cells which support the vital function of eliminating infection among many others [5–8]. A comprehensive understanding of the mechanisms and biochemical pathways governing HSPC regeneration is essential for developing life-saving medical countermeasures (MCMs) against H-ARS and mitigating radiation injuries in clinical applications where radiation is used.

The BM microenvironment consists hematopoietic, vascular, and stromal niches which support and nurture each other [9–11]. HSPCs can be broadly classified into myeloid progenitor cells (MPC) and lineage<sup>-</sup>, Sca-1<sup>+</sup>, c-kit<sup>+</sup> (LSK) cells. The LSK population consists of short-term ‘cycling’ HSCs (ST-HSCs) and long-term ‘quiescent’ HSCs (LT-HSCs) [12–14]. For non-hematopoietic cells, the vascular niche is comprised of endothelial progenitor cells (EPCs) and endothelial cells (ECs) that release canonical niche factors such as stem cell factor (SCF), CXCL12, and angiopoietin-1 to support HSPCs [14–21]. Additionally, the BM vascular niche can be divided into the sinusoidal niche, harboring both quiescent and proliferative HSCs and serving as the main site of BM entry and egress; and the arteriolar niche, supporting quiescent HSCs around small arterioles near the endosteal region of the BM [5, 12, 22]. Furthermore, perivascular mesenchymal stromal cells (MSCs) belonging to the stromal niche represent a small, but essential part of the CD45<sup>-</sup>TER-119<sup>-</sup>CD31<sup>-</sup> (triple negative cells; TNC) fraction in the BM [23]. MSCs secrete growth factors and chemokines such as vascular endothelial growth factors (VEGFs), CXCL12, and SCF that support both BM ECs and HSPCs [24, 25]. High doses of ionizing radiation are known for inducing vascular injury; however, in-depth mechanistic studies focused on BM vascular niche injury

have been limited, even more so for the stromal niche. Thus, therapeutic strategies aimed at mitigating BM vascular and stromal damage are currently lacking.

Thrombopoietin (TPO), a glycoprotein hormone and pleiotropic growth factor, binds to its receptor, c-MPL, expressed on megakaryocytes, platelets, and HSPCs [26–28]. TPO’s primary biological function is to stimulate the generation of platelets [29, 30]. Clinical use of recombinant human TPO (rhTPO) for treating immune thrombocytopenia was discontinued due to subjects developing endogenous neutralizing antibodies, leading to immune-mediated thrombocytopenia [31]. Consequently, a class of drugs with low immunogenicity, referred to as TPO mimetics, were developed to stimulate c-MPL signaling [32]. JNJ-26366821, a TPO mimetic peptide (hereafter referred to as TPOm), is comprised of 29-amino acids conjugated to polyethylene glycol moieties with no sequence homology to endogenous TPO [33, 34]. Both rhTPO and other TPO mimetics, including JNJ-26366821, have demonstrated efficacy in mitigating H-ARS in murine and non-human primate models [35–39]. Currently, the impact of TPO on the BM vascular and stromal niches for HSPC regeneration after irradiation has remained largely unexplored.

In this study, we hypothesized that TPOm will promote regeneration of endothelial and stromal cells in the BM to facilitate hematopoietic recovery after TBI. As such, we investigated the impact of TPOm on megakaryocytes, hematopoietic, endothelial, and stromal cell populations in the BM of healthy and TBI mice using histopathology and flow cytometry. We evaluated the efficacy of TPOm given subcutaneously 24 h post-irradiation in enhancing the survival of TBI mice exposed to varying doses of <sup>137</sup>Cs and X-rays. In addition, we applied in situ whole-mount confocal microscopy to examine the effect of TPOm on the architecture of the arteriolar and sinusoidal vessels with high spatio-temporal resolution in the BM. We also measured the levels of VEGF-A and C in the BM and serum and employed IVIS (In Vivo Imaging System) to evaluate TPOm’s effect on vascular permeability post-TBI. Lastly, we analyzed the effects and interactions of MSCs in the CD45<sup>-</sup>TER-119<sup>-</sup>CD31<sup>-</sup> (triple negative cells; TNC) fraction with other hematopoietic TNCs using single-cell RNA-sequencing (scRNA-seq). This study is the first to reveal a novel activity of TPOm

in fostering the interactions between MSCs and other progenitors within the BM, thereby sustaining BM vasculature and niche homeostasis, leading to HSPC regeneration and mitigation of H-ARS.

## Results

### TPOm expands hematopoietic, endothelial, and stromal cells in murine bone marrow at homeostasis

To confirm the biological activity of TPOm through the TPO/*c*-MPL pathway, we initially measured platelets in the peripheral blood of normal C57BL/6J mice on days 1, 3, 6, and 13 following a single subcutaneous (*sc*) injection of TPOm dosed at 0.3 mg/kg. As expected, platelets (PLT) gradually increased over time, reaching a 3.2-fold peak compared to naïve 6 days after TPOm treatment (Fig. 1A). Furthermore, the numbers of white blood cells (WBC), neutrophils (NE), and lymphocytes (LY) increased ~2.7-fold 3 days after TPOm treatment compared to naïve (Fig. 1B–D). Considering platelets arise from megakaryocytes, we then examined them in the BM after TPOm treatment. Histological analysis of sternal marrow with H&E revealed a significant 2.6- and 3.2-fold increase in megakaryocytes on days 3 and 6 post-TPOm treatment, respectively, compared to naïve (Fig. 1E, F). Morphologically in the TPOm-treated mice, the megakaryocytes are mostly mature, polylobated with abundant cytoplasm. A few young, smaller mononuclear megakaryocytes can also be visualized with rare mitoses. The number of megakaryocytes in the TPOm-treated mice returned to baseline by day 13 (Fig. 1F).

As the number of BM megakaryocytes increased following TPOm treatment, we subsequently investigated the expansion of HSPCs in BM. The HSPC populations were assessed by flow cytometry on days 1, 3, 6, and 13 post-TPOm treatment with the gating strategy depicted in Additional file 1: Figure S1A. MPCs (lineage<sup>-</sup> c-kit<sup>+</sup>), exhibited a significant increase on day 1, followed by a significant depletion on day 6 after TPOm treatment relative to naïve mice (Fig. 1G and Additional file 1: Figure S1G). Despite this decrease, there was a significant, transient expansion of MPCs on day 10, returning to baseline by day 13 after TPOm treatment (Fig. 1G and Additional file 1: Figure S1B). The LSK, megakaryocyte progenitors (MkPs), and ST-HSCs (LSK, CD34<sup>+</sup>) exhibited a similar trend to MPCs after TPOm treatment (Fig. 1G and Additional file 1: Figure S1B). Lastly, LT-HSCs (LSK, CD34<sup>-</sup>CD48<sup>-</sup>CD150<sup>+</sup>) only showed a significant increase by days 10 and 13 post-TPOm treatment (Fig. 1G and Additional file 1: Figure S1B).

The BM vascular and stromal niches also plays a crucial role in maintaining and supporting HSPCs at homeostasis. Thus, we investigated the impact of TPOm on EPCs, ECs, and MSCs using flow cytometry on days 1,

3, 6, and 13 post-TPOm treatment with the gating strategy outlined in Additional file 1: Figure S1C. Post-TPOm treatment, EPCs (CD45<sup>-</sup>, TER-119<sup>-</sup>, CD31<sup>+</sup>, CD34<sup>+</sup>, VEGFR2<sup>+</sup>) peaked with a 5.2-fold increase on day 3, while ECs (CD45<sup>-</sup>, TER-119<sup>-</sup>, CD31<sup>+</sup>) peaked with a 4.8-fold increase on day 10 (Fig. 1H and Additional file 1: Figure S1D). Analysis of vascular subsets within ECs, including arteriolar endothelial cells (AECs; CD45<sup>-</sup>, TER-119<sup>-</sup>, CD31<sup>+</sup>, CD62P<sup>-/low</sup>, Sca-1<sup>+</sup>) and sinusoidal endothelial cells (SECs; CD45<sup>-</sup>, TER-119<sup>-</sup>, CD31<sup>+</sup>, CD62P<sup>+</sup>, Sca-1<sup>-/low</sup>), revealed a significant increase by day 3 post-TPOm injection, with SECs peaking on day 10 (Fig. 1H and Additional file 1: Figure S1D). Further, MSCs (CD45<sup>-</sup>, TER-119<sup>-</sup>, CD31<sup>-</sup>, CD51<sup>+</sup>, CD140α<sup>+</sup>) were acutely expanded on days 1 and 3 after TPOm treatment, returning to baseline by day 6 (Fig. 1H). These findings collectively demonstrate that TPOm effectively increases megakaryocytes and HSPCs in vivo. Remarkably, endothelial and stromal cells in the BM of healthy mice also expanded after TPOm treatment suggesting a broader effect of TPOm on the niche.

### TPOm preserves murine bone marrow architecture and facilitates recovery of hematopoietic, endothelial, and stromal cells after sublethal irradiation

Having established TPOm's capacity to expand HSPC, EC, and MSC populations in the BM of healthy mice, we subsequently investigated its potential to restore the BM of mice subjected to sublethal TBI. Following TBI with <sup>137</sup>Cs dosed at 7 Gy, mice received a single *sc* dose of TPOm at 0.3 mg/kg 24 h post-irradiation and assessed on days 2, 4, 7, and 14 post-TBI. First, the integrity of BM in irradiated mice was examined over time by H&E histology. On day 2 post-TBI, no gross differences were observed between vehicle- and TPOm-treated mice (Fig. 2A). On day 4 post-TBI, the size and extent of hemorrhage in the vehicle-treated mice were greater than the TPOm-treated mice (Fig. 2A). On day 7 post-TBI, early hematopoietic regeneration was evident near the endosteum in TPOm-treated mice, while not yet found in the vehicle-treated mice (Fig. 2A). Lastly, on day 14 after TBI, expansion of megakaryocytes was observed in the sternbrae of TPOm-treated mice, but not as prominently in the vehicle (Fig. 2A, B). Morphologically, the megakaryocytes resemble those present in the non-irradiated mice after TPOm treatment (Fig. 1E). Moreover, an increase in adipocytes was noted in the irradiated marrow on day 14 in both groups (Fig. 2A). Quantifying adipocytes using MarrowQuant [40] identified more adipocytes in the vehicle-treated BM relative to the TPOm-treated BM on day 14 (Fig. 2C). Assessment of cellularity, determined by counting live cells per femur, indicated a significant recovery on day 21 after TBI in the TPOm-treated mice,

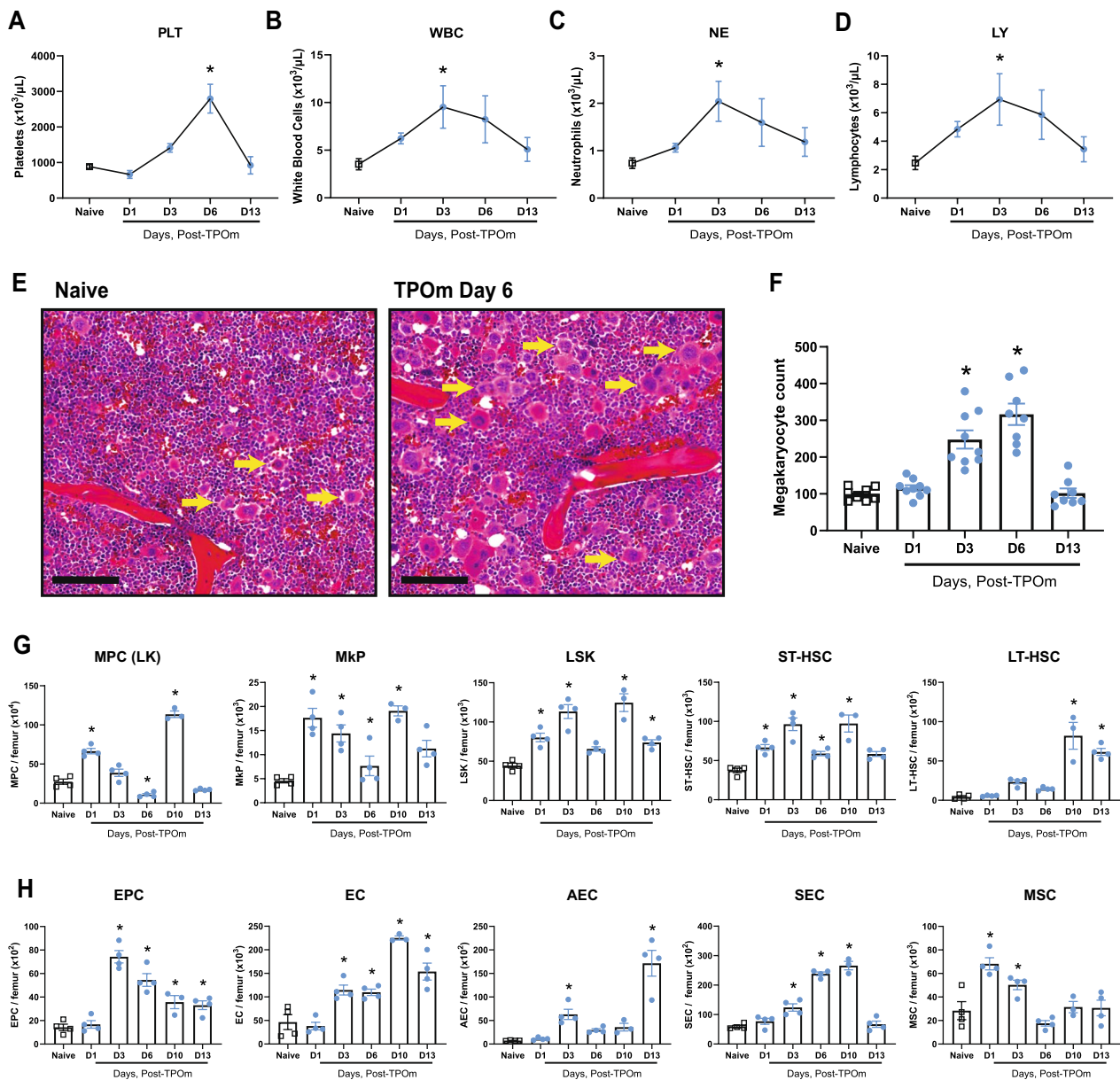


**Fig. 1** TPOm expands megakaryocytes, hematopoietic stem and progenitor, endothelial, and stromal cells in murine bone marrow at homeostasis. **A–D** Complete blood count of peripheral blood for **A** platelets, **B** white blood cells, **C** neutrophils, and **D** lymphocytes. **E** Representative H&E images of sternal bone marrow from naïve and mice treated with TPOm on day 6 after injection. Yellow arrows, megakaryocytes. Scale bar is 100  $\mu\text{m}$ . **(F)** Count of megakaryocytes in the sternal bone marrow of naïve and TPOm-treated mice at the indicated day post-injection ( $n = 3/\text{group}$ ). **(G)** The number of MPC, MkP, LSK, ST-, and LT-HSC per femur of naïve and TPOm-treated mice ( $n = 3\text{--}4/\text{group}$ ) over time. **(H)** The number of EC, EPC, AEC, SEC, and MSC per femur of naïve and TPOm-treated mice ( $n = 3\text{--}4/\text{group}$ ) over time. Data are expressed as mean  $\pm$  SEM. \* $p < 0.05$  vs. naïve assessed by one-way ANOVA with post hoc Dunnett test for multiple comparisons

showing a 3.8-fold increase relative to vehicle-treated (Fig. 2D).

To precisely evaluate the impact of irradiation with and without TPOm on HSPC, EC, and MSC populations in the BM, we conducted flow cytometry. In TPOm-treated mice, the frequency of MPCs significantly increased by

day 10 after irradiation (Additional file 1: Figure S2A), while the absolute count surpassed that of the vehicle-treated mice from day 7 through day 21 after TBI (Fig. 2E). Similarly, the absolute count of MkPs in TPOm-treated mice significantly exceeded that in vehicle-treated mice from day 7 to day 21 after TBI, excluding day 14

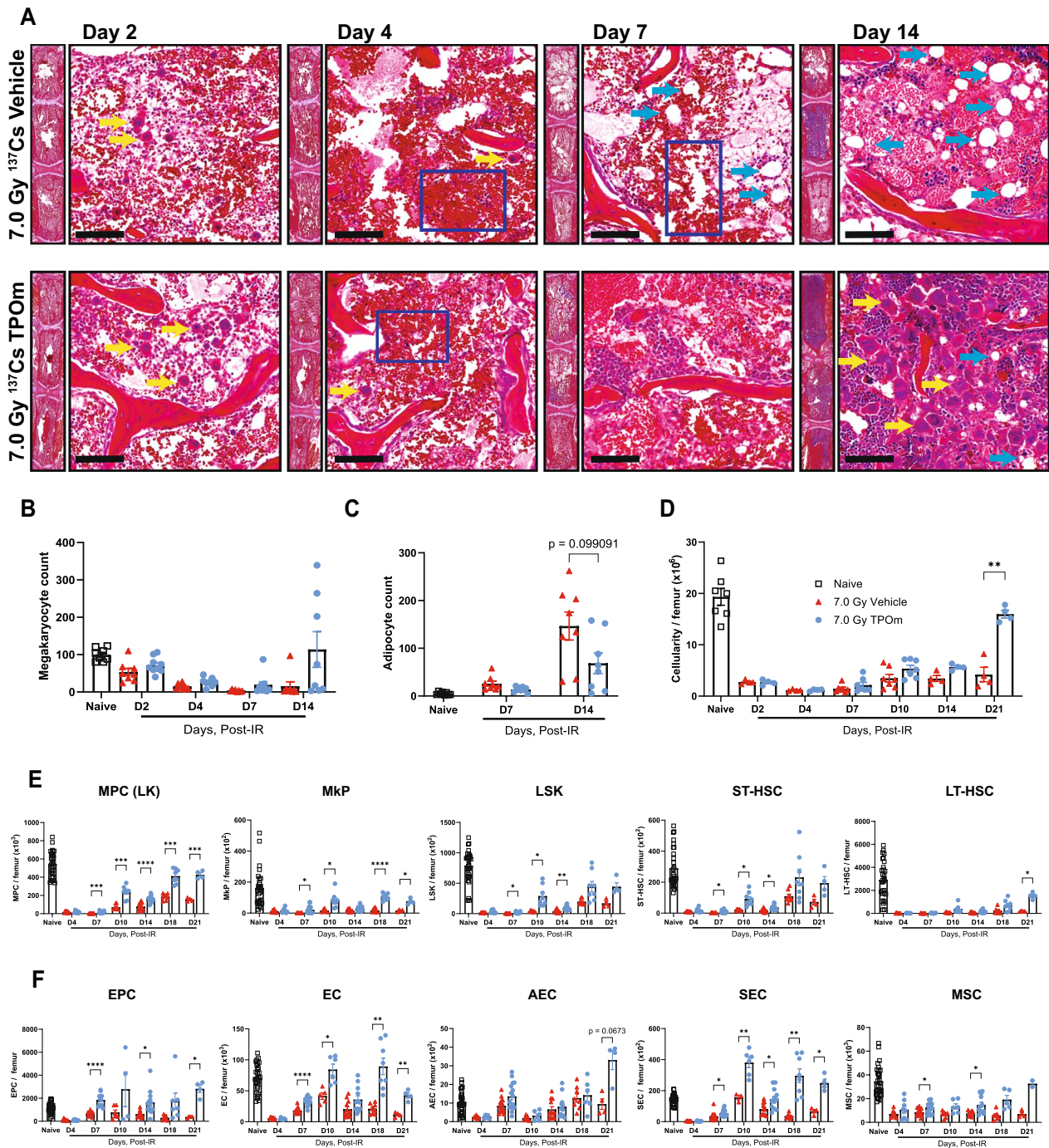


**Fig. 2** TPOm promotes recovery of hematopoietic stem and progenitor, endothelial, and stromal cells in murine bone marrow following 7.0 Gy sublethal total body irradiation. **A** Representative H&E images of sternal bone marrow from vehicle and TPOm-treated mice on days 2, 4, 7, and 14 after irradiation. Yellow arrow, megakaryocytes; light blue arrow, adipocytes; dark blue box, hemorrhaging. Scale bar is 100  $\mu$ m. **B** The number of megakaryocytes in the sternal bone marrow of naive, vehicle, and TPOm-treated mice over time ( $n=3$ /group). **C** The number of adipocytes using MarrowQuant through QuPath in the sternal bone marrow of naive, vehicle, and TPOm-treated mice over time ( $n=3$ /group). **D** Live cell count of femoral bone marrow of naive, vehicle, and TPOm-treated mice over time ( $n=4$ /group). **E** The number of MPC, MKP, LSK, ST-, and LT-HSC per femur of naive, vehicle, and TPOm-treated mice ( $n=4-29$ /group) over time. **F** The number of EC, EPC, AEC, SEC, and MSC per femur of naive, vehicle, and TPOm-treated mice ( $n=4-29$ /group) over time. Data are expressed as mean  $\pm$  SEM.  $*p < 0.05$ ,  $**p < 0.01$ ,  $***p < 0.001$ ,  $****p < 0.0001$  vehicle vs. TPOm-treated assessed by unpaired Student's *t*-test with post hoc Holm-Sidak method for multiple comparisons. Outliers were determined using ROUT with a  $Q=0.2\%$

(Fig. 2E). For the LSK population, a significant increase in frequency was observed on days 7 and 10 in the TPOM-treated mice (Additional file 1: Figure S2A), while their absolute counts remained elevated through day 14 relative to vehicle-treated mice (Fig. 2E). ST-HSCs exhibited a similar trend to LSK cells (Fig. 2E). Conversely, for the rare LT-HSCs, a significant increase in both frequency and absolute count was only observed on day 21 after TBI in TPOM-treated mice compared to vehicle-treated mice (Fig. 2E and Additional file 1: Figure S2A).

In the BM vascular and stromal niches, EPCs in TPOM-treated mice exhibited a significant increase in both frequency and absolute count on day 7, compared to vehicle-treated mice (Fig. 2F and Additional file 1: Figure S2B). Total BM ECs showed a significant increase in frequency only on day 7 in TPOM-treated mice compared to the vehicle-treated mice (Additional file 1: Figure S2B). Moreover, the absolute count of total ECs in TPOM-treated mice was significantly higher than the vehicle-treated mice from days 7 through 21, with a trend for higher counts on day 14 that was not significant (Fig. 2F). For the subsets of ECs, the absolute count of AECs showed no statistical difference between vehicle- and TPOM-treated mice, while the absolute count of SECs significantly increased in TPOM-treated mice from day 7 through day 21 (Fig. 2F). Finally, the absolute count of MSCs also significantly increased on days 7 and 14 in TPOM-treated mice compared to the vehicle-treated mice after TBI (Fig. 2F). These results emphasize TPOM's role in stimulating repopulation and regeneration of HSPCs, ECs, and MSCs in the BM, thereby contributing to the preservation of the BM architecture in mice after sublethal irradiation.

#### TPOM increases survival of mice exposed to lethal irradiation

As TPOM demonstrates the capability to mitigate BM damage in mice following sublethal irradiation, we explored its potential as a radiation MCM for H-ARS. The primary endpoint for evaluating the efficacy of a radiation MCM candidate in animal models is by assessing its impact on the 30-day survival post-lethal TBI. To evaluate the efficacy of TPOM, C57BL/6J mice were irradiated with lethal dose of TBI at 8.8 Gy from a  $^{137}\text{Cs}$  source. This radiation dose was selected because 8.8 Gy TBI is the lethal dose for 70% ( $\text{LD}_{70}$ ) of mice within 30 days post-TBI. Twenty-four hours post-TBI, mice received a single *sc* dose of TPOM at 0.3 mg/kg or vehicle. As illustrated in Fig. 3A, TPOM treatment significantly increased the survival from 28.6% in vehicle-treated mice to 93.3% in the TPOM-treated mice. Moreover, TPOM treatment significantly prevented body weight loss compared to the vehicle-treated mice (Fig. 3B).

We further assessed the efficacy of TPOM in enhancing survival in mice exposed to X-ray TBI. The dose of  $\text{LD}_{100}$  using orthovoltage X-rays is lower than  $^{137}\text{Cs}$ , as established in our previous publication [41]. Notably, a significant increase in survival was observed in male mice exposed to 6.7 and 7.2 Gy TBI ( $\text{LD}_{50}$  and  $\text{LD}_{100}$ , respectively) with TPOM treatment compared to the vehicle-treated mice (Fig. 3C, E). Additionally, the male surviving mice maintained their body weight after irradiation (Fig. 3D, F). In female mice, TPOM improved the survival from 10 to 50% post-7.2 Gy TBI, although it was not statistically significant (Additional file 1: Figure S3A,  $p=0.0681$ ). Moreover, there was no significant difference in the percentage of body weight loss between vehicle- and TPOM-treated TBI female mice (Additional file 1: Figure S3B).

Upon closer examination of BM damage after 8.8 Gy ( $^{137}\text{Cs}$ ) TBI by H&E histology, we noted a substantial reduction in BM cellularity in both vehicle- and TPOM-treated mice on day 4 (Additional file 1: Figure S3C). On day 14 after TBI, sinusoidal dilatation was evident in both groups. However, TPOM-treated mice exhibited more defined, intact vessels, known as BM angiectasis. In contrast, vehicle-treated mice displayed extensive hemorrhaging of the vessels with erythrocytes present in the parenchyma, indicating compromised BM sinusoids (Additional file 1: Figure S3C). Overall, these data demonstrate that TPOM can serve as a potent radiation MCM by increasing the survival of mice exposed to a lethal dose of radiation from various sources.

#### TPOM accelerates and promotes restoration of the vascular niche in mice after lethal irradiation

Extensive vascular dilatation and an increase in vascular area in the diaphysis are inherent responses to BM stress and injury, particularly for the BM sinusoids [9]. Therefore, we investigated the sinusoidal niche *in situ* using whole-mount confocal microscopy of the femur. BM SECs were identified by vascular endothelial growth factor receptor 3 (VEGFR3) labeling, which is exclusively expressed on the BM sinusoids (Fig. 4A). Combined labeling of CD31 and CD144 was employed to examine the total BM vasculature, with DAPI used for nuclei identification in mice irradiated at 8.8 Gy ( $^{137}\text{Cs}$ ) TBI. The VEGFR3<sup>+</sup>-stained area in naïve mice was  $19.8 \pm 1.45 \times 10^3 \mu\text{m}^2$  (Fig. 4A, B). By day 4 after irradiation, this area increased to  $53.7 \pm 2.30 \times 10^3 \mu\text{m}^2$  in vehicle-treated mice, while TPOM significantly inhibited the dilatation to  $43.3 \pm 2.39 \times 10^3 \mu\text{m}^2$  (Fig. 4A, B). Furthermore, by day 10, the VEGFR3<sup>+</sup>-stained area of vehicle-treated mice reached  $45.7 \pm 3.36 \times 10^3 \mu\text{m}^2$ , while with TPOM, it was further reduced to  $35.6 \pm 2.08 \times 10^3 \mu\text{m}^2$  (Fig. 4A, B).

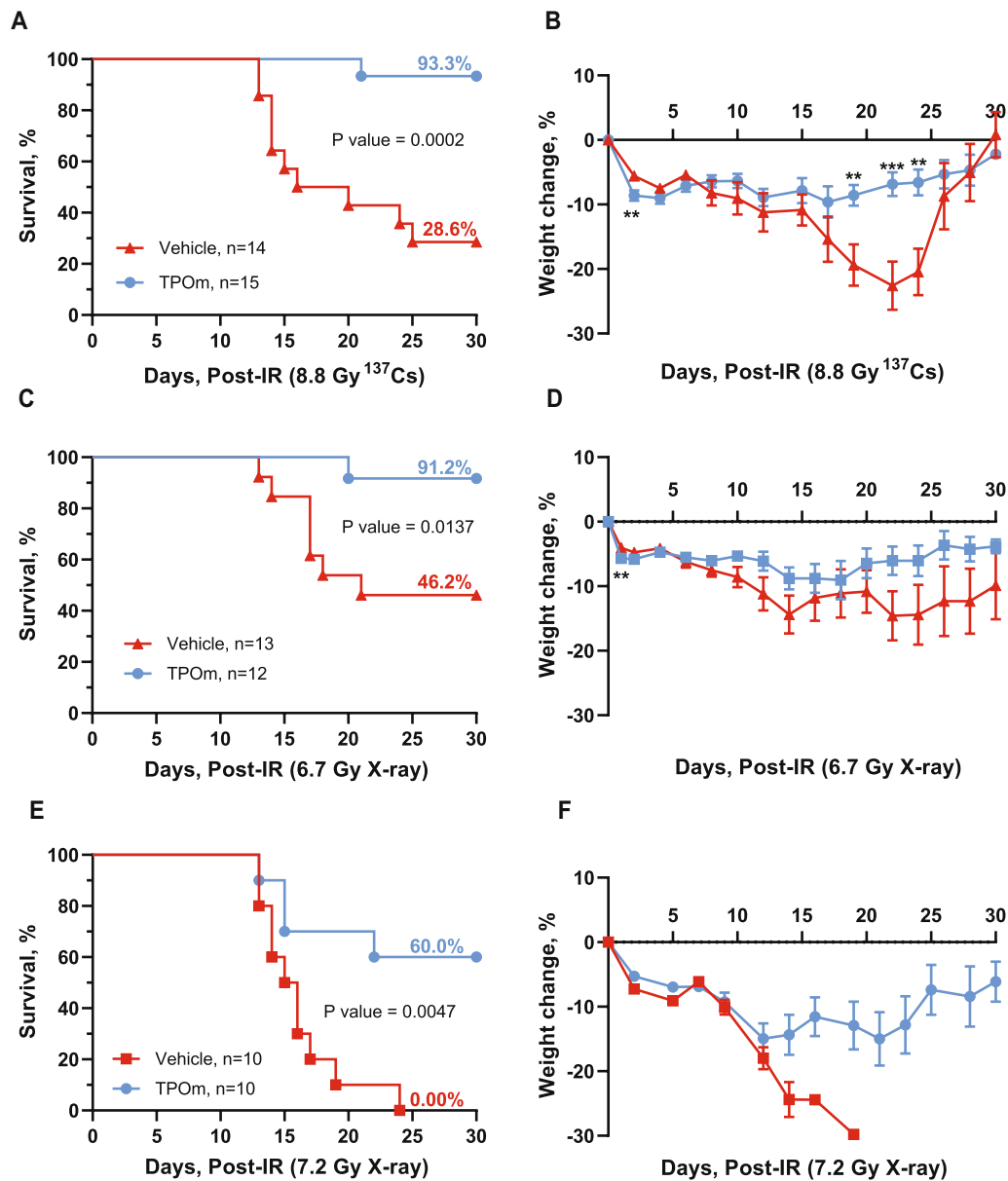


**Fig. 3** TPOM significantly increases survival of mice after lethal total body irradiation. Kaplan–Meier survival curve of vehicle and TPOM treated male mice for 30 days after **A** 8.8 Gy  $^{137}\text{Cs}$ , **C** 6.7 Gy X-ray, and **E** 7.2 Gy X-ray TBI. The percentage of body weight change over 30 days after **B** 8.8 Gy  $^{137}\text{Cs}$ , **D** 6.7 Gy X-ray, and **F** 7.2 Gy X-ray TBI. For survival, the Log-rank (Mantel-Cox) test was used for curve comparison. For the percent weight change data are expressed as mean  $\pm$  SEM. \* $p < 0.05$ , \*\* $p < 0.01$ , \*\*\* $p < 0.001$ , vehicle vs. TPOM-treated by unpaired Student's *t*-test with post hoc Holm-Sidak method for multiple comparisons

These results demonstrate that TPOM enhances the restoration of BM sinusoids in irradiated animals.

To assess the effect of lethal TBI at 9.0 Gy ( $^{137}\text{Cs}$ ) on the arteriolar niche, we used angiopoietin-1 receptor, known as TIE2, as a marker to distinguish AECs, given their high expression of TIE2 [42]. BM arterioles also express Sca-1, typically a marker of for hematopoietic progenitors (Additional file 1: Figure S1A). On days 2

and 4 after TBI, arterioles, marked as Sca-1<sup>+</sup> and TIE2<sup>+</sup>, were readily detected in both naive and irradiated mice and appeared unchanged (Fig. 4C). Moreover, on day 4, the Sca-1<sup>+</sup> hematopoietic cells were found more clustered in the TPOM-treated mice compared to the vehicle, particularly around the arterioles (Fig. 4C). The number of Sca-1<sup>+</sup> cells in the vehicle mice began to decrease on day 2 and further decreased on day 4, compared to the

naïve (Fig. 4D). In contrast, the number of Sca-1<sup>+</sup> cells in the TPOM-treated mice were well maintained, reaching a level similar to the naïve mice and significantly higher than the vehicle ( $637 \pm 41$  vs.  $1150 \pm 58$  cells per field) on day 2, although it dropped to similar counts as the vehicle on day 4 (Fig. 4D). Despite not detecting noticeable changes in the BM arterioles after irradiation, there were increased numbers of Sca-1<sup>+</sup> cells near the endosteum and arterioles in TPOM-treated mice.

To further analyze the impact of TPOM on vascular integrity and function, we utilized IVIS imaging to evaluate vascular permeability. Mice were exposed to 7.2 Gy TBI with X-rays, followed by TPOM treatment 24 h post-irradiation. On day 3 after irradiation, mice received an injection of a vascular dye (AngioSense 750EX) intravenously and were imaged 48 h later. The IVIS imaging showed that there was a greater amount of dye present in the tissues of the vehicle-treated mice compared to the TPOM-treated mice (Fig. 4E). After quantification of the region of interests (ROIs), the total radiant efficiency in the TPOM-treated group was significantly lower than the vehicle-treated group by 53.2% (Fig. 4F). These findings suggest that TPOM contributes to vascular integrity, as evidenced by the reduced leakage of vascular dye into surrounding tissues.

VEGFs play a crucial role in regulating ECs, influencing growth and repair processes [43]. Consequently, we investigated the effect of TPOM on the levels of VEGF-A and VEGF-C in the BM and serum. In healthy mice, following TPOM injection, VEGF-A levels significantly increased on day 3 in serum and on day 13 in the BM (Additional file 1: Figure S4A, B). Concurrently, VEGF-C levels significantly increased on days 1 and 3 in the BM and serum, respectively, after TPOM treatment (Additional file 1: Figure S4C, D). However, when mice were subjected to 7 Gy (<sup>137</sup>Cs) TBI, TPOM treatment did not elevate VEGF-A levels in either serum or BM, unlike healthy mice (Fig. 4G, H). Nevertheless, the levels of VEGF-C in the BM and serum of TPOM-treated mice were markedly increased on days 2 and 4, respectively,

compared to the vehicle-treated and naïve mice (Fig. 4I, J). These results highlight that TPOM can selectively stimulate the release of VEGFs, distinctively VEGF-C, both systemically and locally, promoting the repair of vascular damage in the BM and potentially other organs after irradiation.

#### TPOM elicits distinct changes in cellular heterogeneity and cell cycle dynamics of murine bone marrow cells post-irradiation evaluated by single-cell RNA-sequencing analysis

BM MSCs play a significant role in the regeneration of HSPCs and ECs, particularly after irradiation [24, 44]. Given the observed increase in MSCs after TPOM treatment (Figs. 1H and 2F), we further investigated the effect of TPOM on MSCs. We sorted BM from mice using the markers CD45<sup>-</sup>, TER-119<sup>-</sup>, and CD31<sup>-</sup> [triple negative cells (TNC)] [23, 45] as this fraction is enriched for MSCs and conducted single-cell RNA-sequencing. Mice were divided into four groups: naïve, TPOM alone, 6 Gy TBI (X-rays), and 6 Gy TBI followed by TPOM treatment 24 h post-irradiation. BM was harvested on day 10 after irradiation. A heatmap of the top 10 enriched genes was generated for each cluster to identify the populations of TNCs (Fig. 5A). An overall UMAP was generated by combining clusters from all four groups (Fig. 5B) as well as individual UMAPs for each group (Fig. 5C). Notably, neutrophil progenitors (Neutro\_prog), megakaryocyte progenitors (Mk\_prog), and eosino-basophil progenitors (Eo-Baso\_prog) were noticeably depleted after irradiation, while Pro-B cells and both clusters of erythroblasts were increased (Fig. 5C). Analyzing the percentage of each cluster per group revealed that TPOM alone increased the percentage of Neutro\_prog and Mk\_prog from 32.9% to 38.5% and 13% to 17.9%, respectively, compared to naïve (Fig. 5D). Following irradiation, most identified clusters, with the exception of Pro-B cells, were increased after TPOM treatment relative to the irradiation alone group (Fig. 5D).

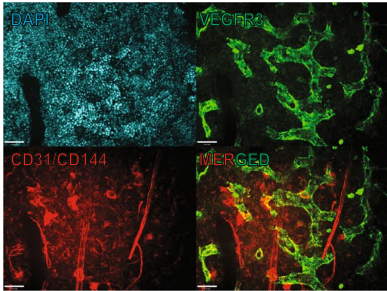
(See figure on next page.)

**Fig. 4** TPOM systemically reduces bone marrow vascular dilatation and vascular leakage and promotes production of VEGF-A and VEGF-C in irradiated mice. **A** Representative immunofluorescent images of femurs stained with DAPI (blue), VEGFR3 (green), and CD31/CD144 (red) on days 4 and 10 after irradiation in vehicle and TPOM-treated mice. Non-irradiated mice were represented as naïve for reference. Scale bar is 10  $\mu$ m. **B** VEGFR3<sup>+</sup> vessel area in the bone marrow on days 4 and 10 after irradiation, quantitated by using Volocity software (n = 3/group). **C** Representative immunofluorescent images of sternum stained with DAPI (blue), Sca-1 (green), and TIE2 (red) on days 2 and 4 after irradiation in vehicle and TPOM-treated mice from 2 independent experiments. Non-irradiated mice were represented as naïve for reference. **D** Quantification of Sca-1<sup>+</sup> cells per 100 $\times$  field in sternal bone marrow quantitated by using Volocity software (n = 3/group). **E** IVIS images of 7.2 Gy (X-rays) TBI mice imaged 5 days after irradiation with AngioSense750 EX i.v. injection performed on day 3 after irradiation. **F** Quantification of total radiant efficiency (n = 3/group). **G, H** ELISA of VEGF-A in **(G)** serum and in **(H)** BM after 7.0 Gy (<sup>137</sup>Cs) TBI. **I, J** ELISA of VEGF-C in **(I)** serum and in **(J)** BM after 7.0 Gy (<sup>137</sup>Cs) TBI. Data are expressed as mean  $\pm$  SEM. \**p* < 0.05, \*\**p* < 0.01 vehicle vs. TPOM-treated assessed by unpaired Student's *t*-test with post hoc Holm-Sidak method for multiple comparisons

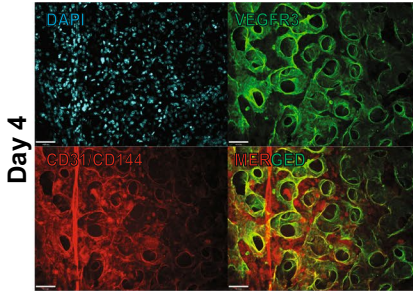


**A**

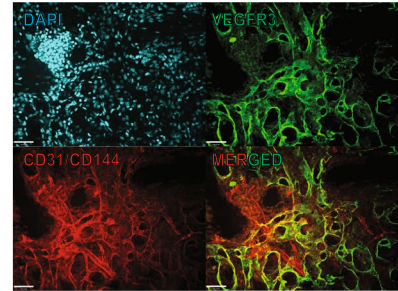
**Naive**



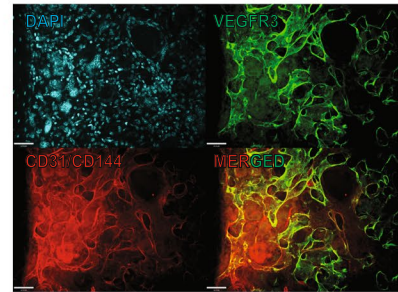
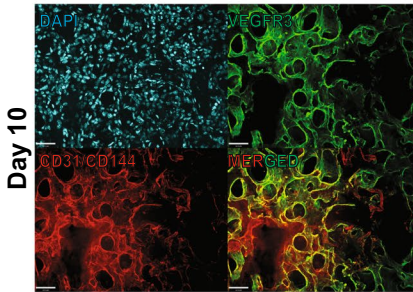
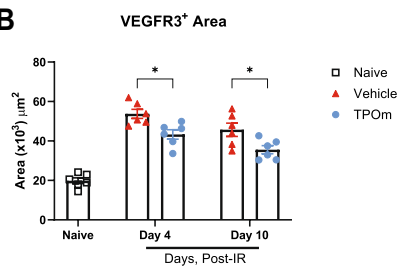
**8.8 Gy <sup>137</sup>Cs Vehicle**



**8.8 Gy <sup>137</sup>Cs TPOM**

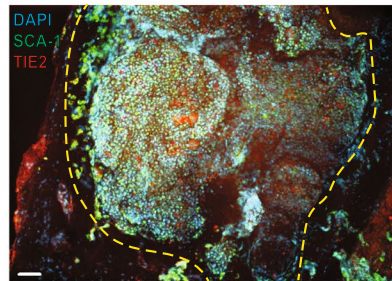


**B**

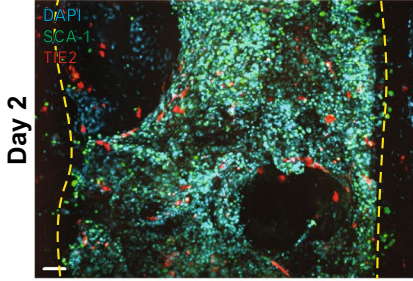


**C**

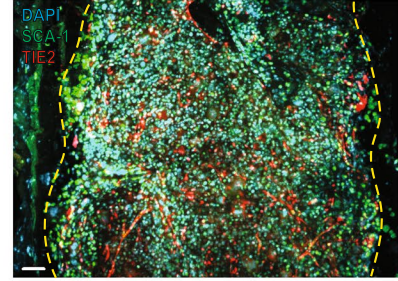
**Naive**



**9.0 Gy <sup>137</sup>Cs Vehicle**



**9.0 Gy <sup>137</sup>Cs TPOM**



**D**

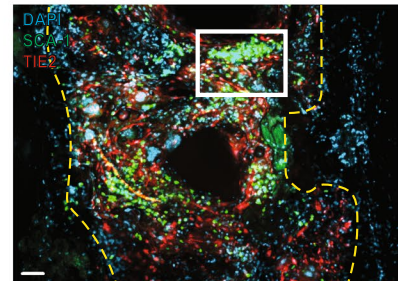
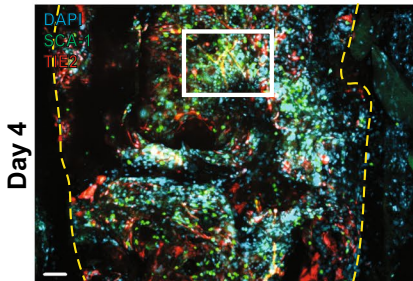
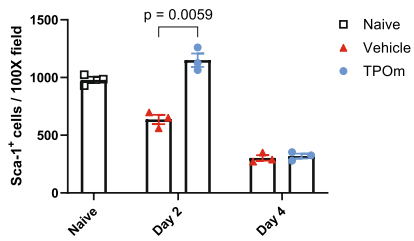


**Fig. 4** (See legend on previous page.)

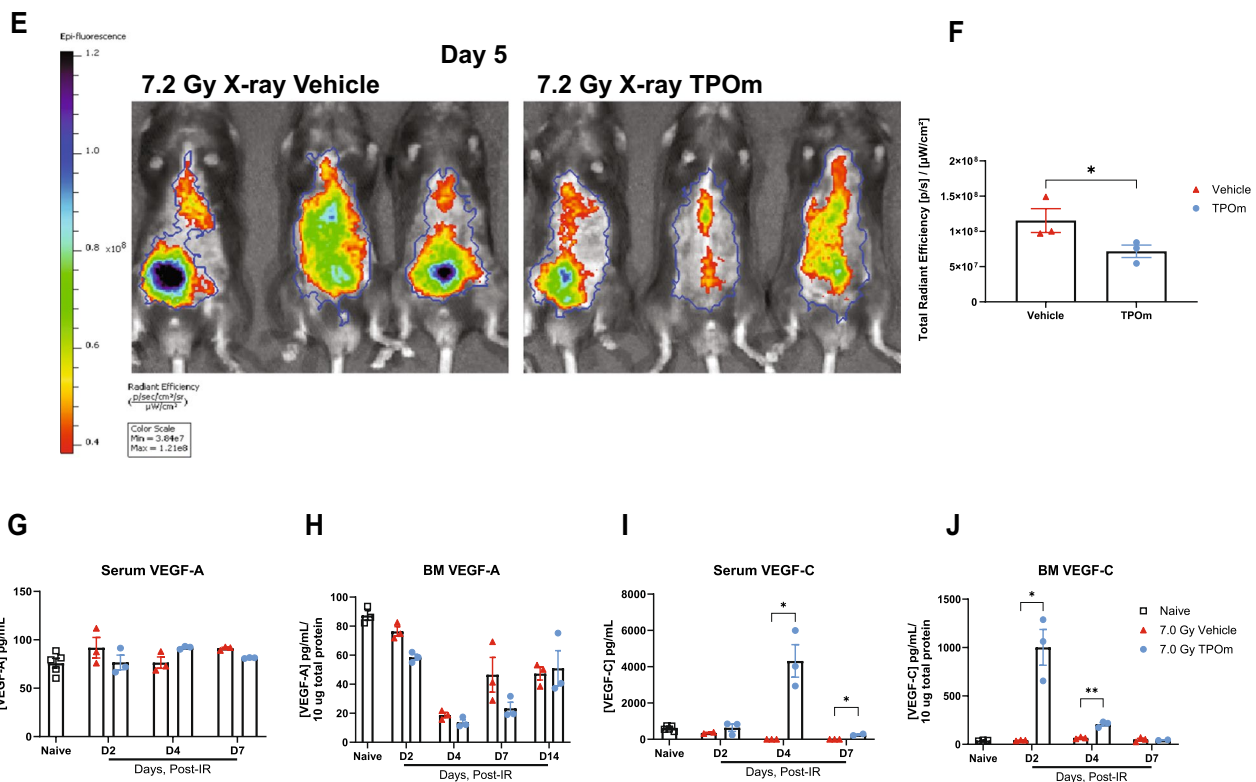


Fig. 4 continued

To further pinpoint clusters demonstrating active proliferation, we analyzed the expression of the proliferation marker *Mki67*. The combined UMAP displayed elevated levels of *Mki67* in the erythroblasts and Pro-B cells (Fig. 5E). As anticipated, TPOM increased *Mki67* expression in Mk\_prog cluster (Additional file 1: Figure S5A). Irradiation increased *Mki67* expression in Neutro\_prog, Mk\_prog, and erythroblast 2 clusters, an effect further amplified in the irradiation plus TPOM-treated group (Fig. 5F and Additional file 1: Figure S5A). Additionally, we assessed the cell cycle status of each cluster for all the individual groups (Additional file 1: Figure S5B). For comparison, the percentage of each cell cycle phase (G1, G2M, or S) in each cluster was plotted for all groups

(Fig. 5G). In healthy mice, TPOM notably increased the percentage of Pro-B cells in the G2M phase, Neutro\_prog in the G1 phase, and erythro-progenitors (Erythro\_prog) in the G1 phase (Fig. 5G). Radiation increased the percentages of several clusters in S phase, while TPOM treatment slightly decreased the percentage of all the Erythro-clusters in the S phase (Fig. 5G). Particularly, MSCs exhibited a slight increase in the S phase after TPOM treatment in the irradiated groups; however, the percentage of MSCs in G2M was increased with TPOM treatment compared to irradiation alone (Fig. 5G). Collectively, these data highlight that TPOM regulates both the proliferation and cell cycle dynamics of erythroid, B lymphoid, and MSCs after irradiation.

(See figure on next page.)

**Fig. 5** TPOM increases subpopulations of hematopoietic progenitors and *Mki67* expression in sorted bone marrow TNCs from mice after sublethal total body irradiation. Single-cell RNA-seq analysis of sorted CD45<sup>+</sup>, TER-119<sup>+</sup>, CD31<sup>-</sup> (TNC) cells derived from BM of mice 10 days after 6 Gy (X-ray) TBI. **A** Heatmap of highly expressed genes used to identify different cell clusters. **B** Overall UMAP clustering of TNC cells, **C** individual UMAP clusters following each group: naive (Control), TPOM alone, irradiated (IR), and irradiated plus TPOM-treated (IR\_TPOM). **D** Each of the cluster's distribution by percentage iterated by treatment condition. **E** Expression distribution of *Mki67* on the overall UMAP of TNC cells. **F** Violin plots of *Mki67* expression iterated by identified clusters per treatment group. **G** Cell cycle analysis of each identified cluster per treatment group

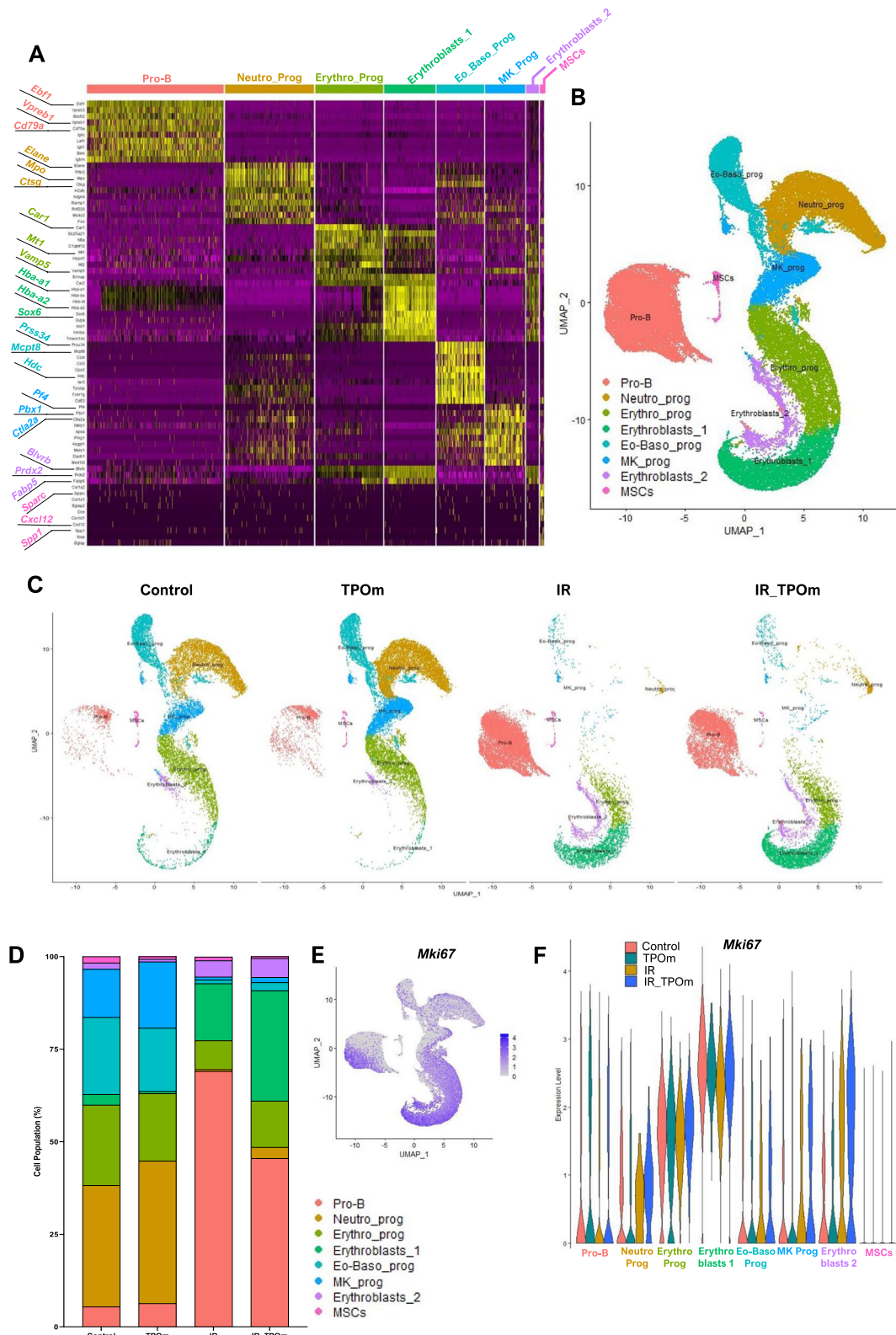


**Fig. 5** (See legend on previous page.)

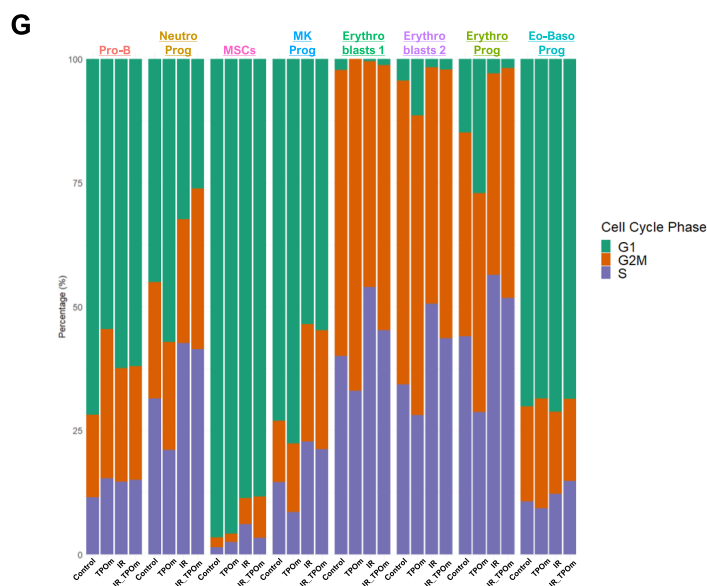


Fig. 5 continued

**TPOm enhances the interaction of mesenchymal stromal cells with other hematopoietic progenitors in the mouse bone marrow after irradiation**

To explore cell–cell interaction among the different clusters, we used the CellChat [46] program to analyze the single-cell RNA sequencing data. The analysis revealed that MSCs acted as a central signaling hub, engaging in robust interactions with other clusters in the dataset (Fig. 6A). Identification of MSCs was based on the expression levels of several genes, including canonical MSC markers such as *Pdgfra* and *Lepr* (Additional file 1: Figure S6A). The predicted ligand–receptor communications from MSCs to each cluster, along with the intensity of these interactions is illustrated in Fig. 6B. Collagens expressed in MSCs emerged as the primary contributors to the cell–cell interactions, with *Col1a2-Cd44* exhibiting the highest contribution (Fig. 6C). *Cd44* was highly expressed in *Neutro\_prog*, *Mk\_prog*, and *Erythro\_prog* (Fig. 6B and Additional file 1: Figure S6B). Another significant molecule in mediating cell–cell interactions

was *Sdc4*, which was highly expressed in Pro-B cells and MSCs (Fig. 6B and Additional file 1: Figure S6B). We further analyzed the expression levels of several genes in the collagen family in each experimental group. In TPOm-treated mice, there was an increased expression of *Col1a1* and *Col1a2* in MSCs, and irradiation also heightened this expression (Fig. 6D). Particularly in the irradiated groups, TPOm treatment increased the expression of *Col1a2*, *Col4a1*, and *Col4a2* in MSCs compared to radiation alone, while it decreased the expression of *Col6a2* (Fig. 6D).

We further explored the expression of genes in MSCs that might be influenced by TPOm treatment. MSCs inherently expressed canonical EC ligands, such as VEGFs, which would contribute to EC regeneration (Additional file 1: Figure S6C). Differential expression analysis between TPOm treatment and naïve mice revealed that one gene, *Col8a1*, was significantly down-regulated, and 12 genes were significantly upregulated, including various collagens and osteoblastic genes

(See figure on next page.)

**Fig. 6** TPOm stimulates the interaction of MSCs with other cell clusters by upregulating the regeneration pathway and collagens expression. **A** Chord diagram of cell-to-cell communications between MSCs and other identified clusters of the TNC in the BM. **B** MSCs (sender) and other identified clusters (receivers) interaction by ligand and receptor. **C** Relative contributions of each ligand–receptor interaction. **D** Violin plots of the expression levels of different collagens expressed by MSCs iterated in each treatment group. **E** Volcano plot of differentially expressed genes of TPOm vs. Naïve groups and **F** Gene Ontology pathways significantly overrepresented among up- and down-regulated genes **G** Volcano plot of differentially expressed genes of irradiated (IR) vs. TPOm-irradiated (IR\_TPOm) groups and **H** Gene Ontology pathways significantly overrepresented among down-regulated genes. Differential expression was performed with MAST model adjusting for Sex, nCount\_RNA, percent.mt, S. Score

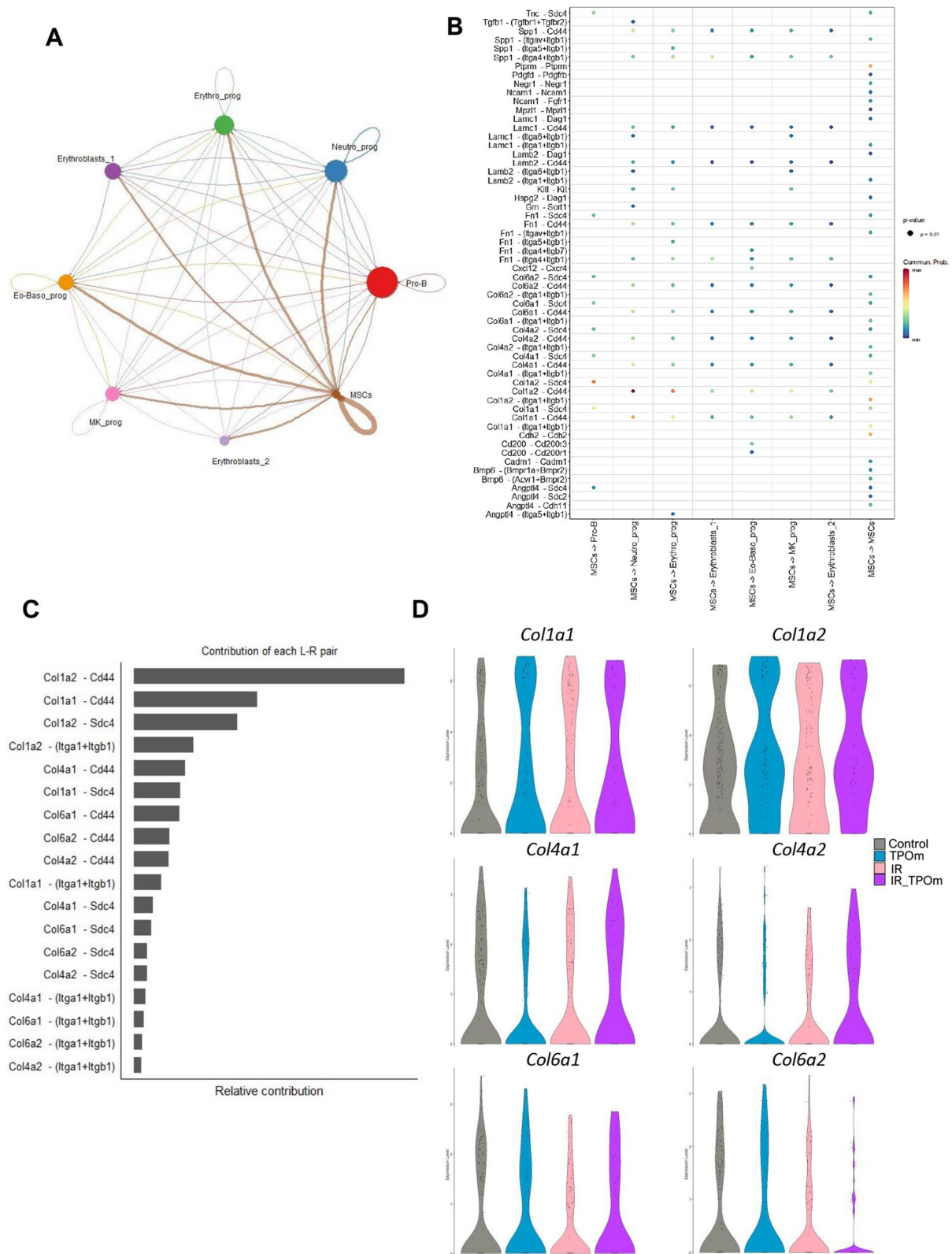


**Fig. 6** (See legend on previous page.)

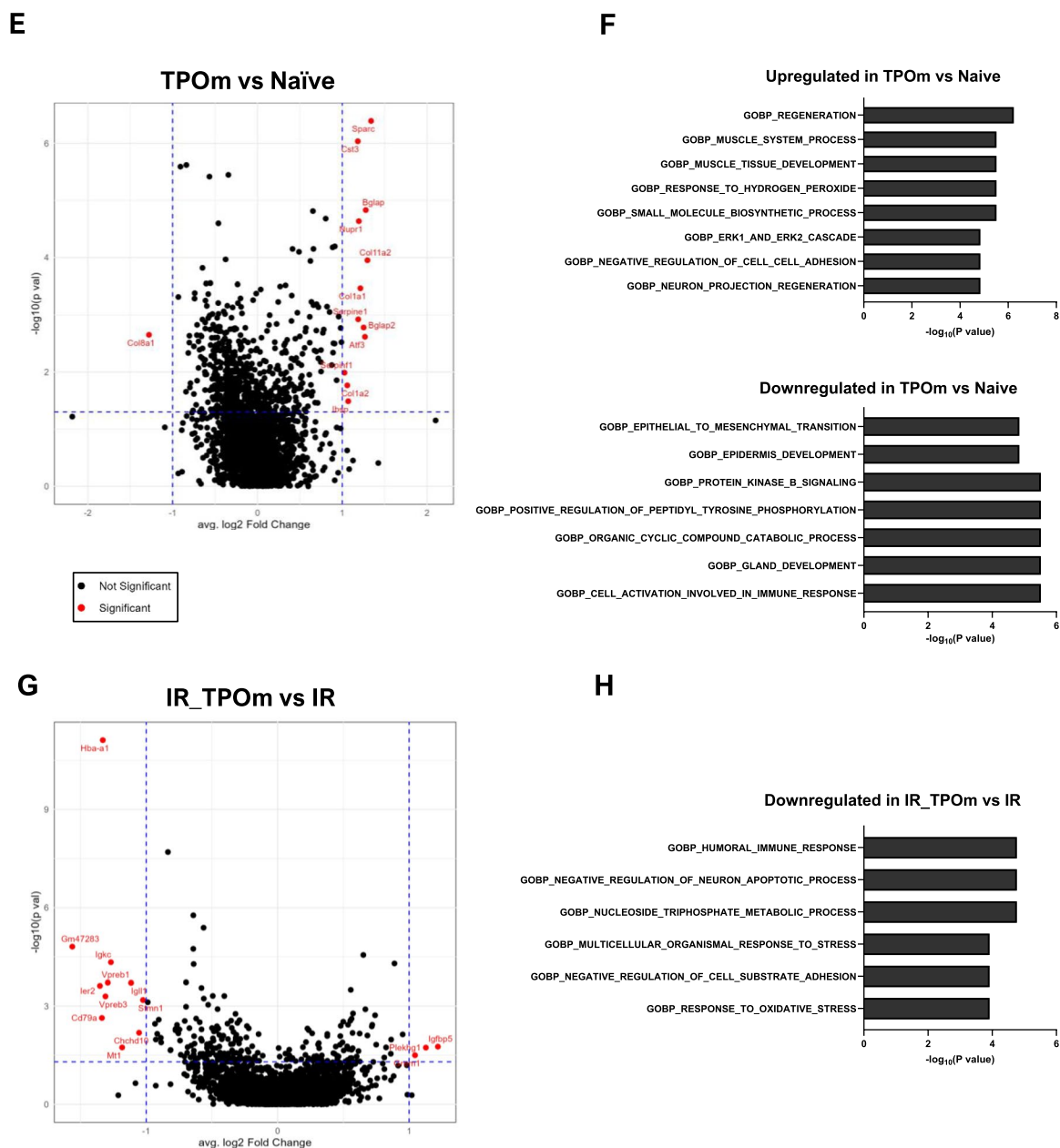


Fig. 6 continued

(Fig. 6E). The single cell pathway analysis (SCPA) using Gene Ontology Biological Pathways database (GOBP) of differentially expressed genes demonstrated a notable increase in the regeneration pathway in TPOm-treated mice compared to naïve (Fig. 6F). When comparing the differential expression between TBI and TBI plus TPOm-treated mice, 11 genes were significantly downregulated, and 3 genes were significantly upregulated (Fig. 6G). The SCPA of these genes indicated that the humoral immune

response, multicellular organismal response to stress, and response to oxidative stress were significantly downregulated in the TPOm-treated mice after TBI (Fig. 6H). Together, these results suggest that TPOm upregulates several genes in the collagen family in MSCs, promoting their interaction with other hematopoietic TNCs in the BM. Moreover, TPOm stimulates regeneration and suppresses the humoral immune response in mice with treatment alone or after TBI, respectively.

## Discussion

In today's geopolitical climate, individuals face the looming threat of exposure to high doses of ionizing radiation due to nuclear or radiological incidents, which carries the risk of developing ARS. In addition, patients undergoing myeloablative BM transplant conditioning suffer from radiation-induced toxicities and mortality. The hematopoietic system, consisting of highly proliferative stem cells, stands out as one of the most susceptible organ to radiation-induced injury [47]. In established animal models for TBI, four FDA-approved drugs targeting the hematopoietic system—Neupogen, Neulasta, Leukine, and Nplate (Romiplostim)—have demonstrated efficacy in increasing HSPCs in irradiated animals [2, 48–50]. However, their activity regulating the BM microenvironment for HSPC regeneration remains unexplored. In this study, we have evaluated the potential of TPOM (JNJ-26366821) as a radiation MCM [37] and agent than can mitigate radiation induced toxicities, focusing on its role in regulating BM vascular and stromal niches for HSPC regeneration in mice exposed to TBI from  $^{137}\text{Cs}$  and X-ray sources.

Our findings show that TPOM effectively expanded HSPCs, ECs, and MSCs in the BM of both healthy and irradiated mice. TPOM also significantly improved the 30-day survival of TBI-exposed mice, a necessary endpoint for evaluating drug efficacy in treating H-ARS according to the FDA animal rule [2]. Furthermore, our study reveals a novel activity of TPOM in alleviating BM vascular dilation in the sinusoidal niche and maintaining the arterioles of the arteriolar niche post-TBI. TPOM reduced vascular permeability, a typical consequence of exposure to high doses of radiation and increased the levels of VEGF-C in BM and serum. scRNA-seq analysis unveiled another novel function of TPOM in upregulating the expression of specific collagens in MSCs, thereby promoting their interaction with other rare hematopoietic progenitors in the BM. Additionally, TPOM upregulated regeneration and dampens the humoral response in MSCs.

We have verified that TPOM exhibited functionality akin to endogenous TPO by exerting its role as a regulator of platelet production from megakaryocytes through the differentiation of HSCs [29]. TPOM was developed by screening peptides capable of binding to c-MPL with a phage display library [51]. After a single *sc* injection, TPOM significantly increased the number of megakaryocytes in the BM of the healthy mice on days 3 and 6 which is in line with its role of promoting Mk differentiation. Moreover, TPOM induced a significant expansion of the HSPCs, consistent with prior studies demonstrating direct binding of TPO to HSCs and the expansion of

LSK cells [52]. Recognizing the critical role of vascular and stromal niches in the BM for HSPC regeneration [9, 24, 44], our study examined the broader effects of TPOM treatment on other constituents of the BM microenvironment. We observed a significant increase in EPCs, ECs, AECs, SECs, and MSCs in the BM of healthy mice post-TPOM treatment. Notably, some organ-specific ECs expressing c-MPL, such as liver sinusoidal ECs and human umbilical vein ECs, have been reported [53, 54] suggesting the potential of direct interactions of ECs with TPOM. Furthermore, investigators have found that BM osteoblasts and -clasts express c-MPL [55]. Osteoblasts are derived from BM MSCs which may explain how TPOM is interacting with MSCs at homeostasis and after irradiation. While our findings point to a potential role of TPOM in the expansion of EC and MSC populations in the BM, the nature of this effect, whether direct or indirect, warrants further investigation.

For mice exposed to TBI at sublethal 7.0 Gy ( $^{137}\text{Cs}$ ) doses, the architecture and cellularity of BM were damaged, reflecting severe depletion of HSPCs, ECs, and EPCs that persisted for at least 14 days after TBI. With TPOM treatment, the architecture and cellularity of BM were more preserved, exhibiting less hemorrhage and adipocytes. A significant recovery of MPCs, LSK cells, and ST-HSCs by day 7 was observed in TBI mice treated with TPOM. Similarly, recent studies demonstrated that endogenous TPO, mainly produced from liver, promotes the regeneration of HSCs after chemo- and radio-induced myeloablation, an example of cross-organ signaling [56, 57]. Moreover, TPOM increased EPCs at day 7 after TBI, which would differentiate into mature ECs, resulting in a marked elevation of EC counts starting from day 10 after TBI.

Next, we evaluated the effectiveness of TPOM as a potential radiation MCM by subjecting mice to lethal doses of radiation: 8.8 Gy ( $^{137}\text{Cs}$ ), 6.7 Gy (X-ray), and 7.2 Gy (X-ray). Administering TPOM 24 h post-TBI resulted in a significant increase in 30-day survival rates at all three radiation doses, exceeding the vehicle-treated mice by at least 45%. Notably, TPOM demonstrated its efficacy not only in male mice but also in improving the survival of female mice exposed to X-ray irradiation. In addition to the enhanced survival rates, TPOM treatment effectively mitigated body weight loss following TBI. This mitigative effect aligns with our previous study, which demonstrated that TPOM significantly increased the survival of CD2F1 and C57BL/6J mice exposed to TBI from a  $^{60}\text{Co}$   $\gamma$ -radiation source in a dose-dependent manner [37]. An important consideration is that various radiation sources, as described in our prior publication, can have significantly different effects on the composition of the BM depending on the dose; as such,  $\gamma$ -radiation and

X-rays at isodoses are not equivalent [41]. In our current study, we administered a single dose of TPOm. Further studies are warranted to explore the pharmacodynamics of TPOm in mice to ascertain if additional doses could further improve survival rates post-TBI.

Our findings are consistent with the activity of other c-MPL agonists in mitigating H-ARS. For instance, administration of rhTPO enhanced the HSPC recovery in irradiated mice and significantly improved the survival of both mice and non-human primates exposed to lethal TBI [58]. Romiplostim, another TPO mimetic recently approved by the FDA to treat patients acutely exposed to myelosuppressive doses of radiation, has also demonstrated its efficacy in conferring a survival benefit in murine and non-human primate models of H-ARS [38, 59, 60]. To our knowledge, this is the first study to examine the role of TPOm in mitigating radiation-induced vascular and stromal injuries to support hematopoietic regeneration, marking a significant advancement in our understanding of TPO's multifaceted mitigative mechanisms.

The vasculature within the BM can be divided into sinusoids and arterioles [17]. In mice exposed to TBI, we observed increased vessel dilation of the sinusoids, quantified by the area of VEGFR3, which was reduced by TPOm treatment. In the arteriolar niche, the structure of arterioles remained intact after lethal irradiation, albeit a marked decrease in the number of Sca-1<sup>+</sup> cells was observed. Previous studies have reported differences in radiosensitivity between sinusoids and arterioles in the BM [9, 13]. The impact of TPOm on vasculature was further evident in the reduction of vascular dye leakage throughout the body of TBI mice, as detected by IVIS imaging. Likewise, we demonstrated that TPOm increased the levels of VEGFs in the BM and serum. Our findings are supported with previous reports indicating that TPO released from BM stromal cells can bind to HSCs to stimulate VEGF, implying a potential role in vascular regeneration [25, 61]. Vascular swelling after irradiation can be alleviated by HSC transplant supplemented with VEGF-A [9], and MSC-secreted VEGF-C has been shown to be crucial in regeneration of the vascular niche after irradiation [24]. Remarkably, TPOm distinctively increased VEGF-C levels within the BM and serum in healthy and irradiated mice. Consequently, TPOm may exert beneficial effects on regeneration and recovery of ECs post-irradiation, which subsequently affects BM HSPCs, potentially through the release of VEGFs.

To investigate the effect of irradiation with and without TPOm treatment on BM MSCs, we isolated the TNCs from the BM using cell sorting for single-cell RNA sequencing. Previous studies have established that the CD45<sup>-</sup>, TER-119<sup>-</sup>, CD31<sup>-</sup> fraction of the BM is enriched

with a heterogeneous population of MSCs and devoid of hematopoietic, erythroid, and endothelial cells [45]. However, recent findings have challenged this notion, revealing that TNCs contain cells of hematopoietic origins, particularly B lymphoid and erythroid lineages, which are dependent on signals from MSCs [23]. Our scRNA-seq data revealed a significant loss of Mk\_prog, Neutro\_prog, and Eo-Baso\_prog populations after irradiation, with TPOm treatment mitigating this loss to some extent. Conversely, B lymphoid and erythroid lineages expanded after irradiation, with the erythroid clusters showing further enhancement with TPOm treatment. One study reveals that B lymphoid lineage and plasma cells derived from BM are resistant to radiation [62]. The elevation of Ter-119<sup>low/-</sup> erythroid cells, a hallmark of stress-erythropoiesis, is typical after irradiation [63]. Further, TPO has been demonstrated to synergize with erythropoietin (EPO) and support erythroid recovery following myeloablative injury [64]. These findings suggest a potential role for TPOm in influencing the dynamics of various hematopoietic lineages post-irradiation.

The scRNA-seq data also uncovered the pivotal role of MSCs as central regulators of various hematopoietic TNCs. Interactions between MSCs and the other clusters were predominantly mediated by Col1a2/Col1a1 and syndecan-4 (Sdc4) or Cd44. Specifically, Sdc4 exhibited high expression on the Pro-B cluster and has been shown to modulate cell migration and adhesion [65]. Alternatively, the Neutro\_prog, Erythro\_prog, and Mk\_prog clusters predominantly interacted with MSCs through Cd44, which is known for its critical functions in cell migration, adhesion, and homing [66]. Moreover, Cd44 has been used to differentiate stages of erythroid lineage development [67]. Sdc4 and Cd44 are known as cell-surface heparan sulfate proteoglycans that are indispensable for humoral immune system development and maintenance of hematopoiesis, in general [68]. These findings collectively suggest that MSCs play a crucial role in maintaining early B lymphoid and erythroid cells, priming them for HSPC recovery after irradiation. It is noteworthy that TPOm appears to augment these interactions, indicating a potential enhancement of MSC-mediated recovery of hematopoietic cells after irradiation.

TPOm has undergone thorough nonclinical toxicology evaluations, including chronic toxicity studies, and no issues have been identified that would preclude its clinical development [33]. A Phase 1 clinical study involving healthy volunteers further supported the safety and tolerability of TPOm. Particularly, TPOm dose-dependently elevated platelet counts and increased total colony-forming unit (CFU) counts compared to the placebo, with no evidence of antibody formation against endogenous TPO in humans [69].



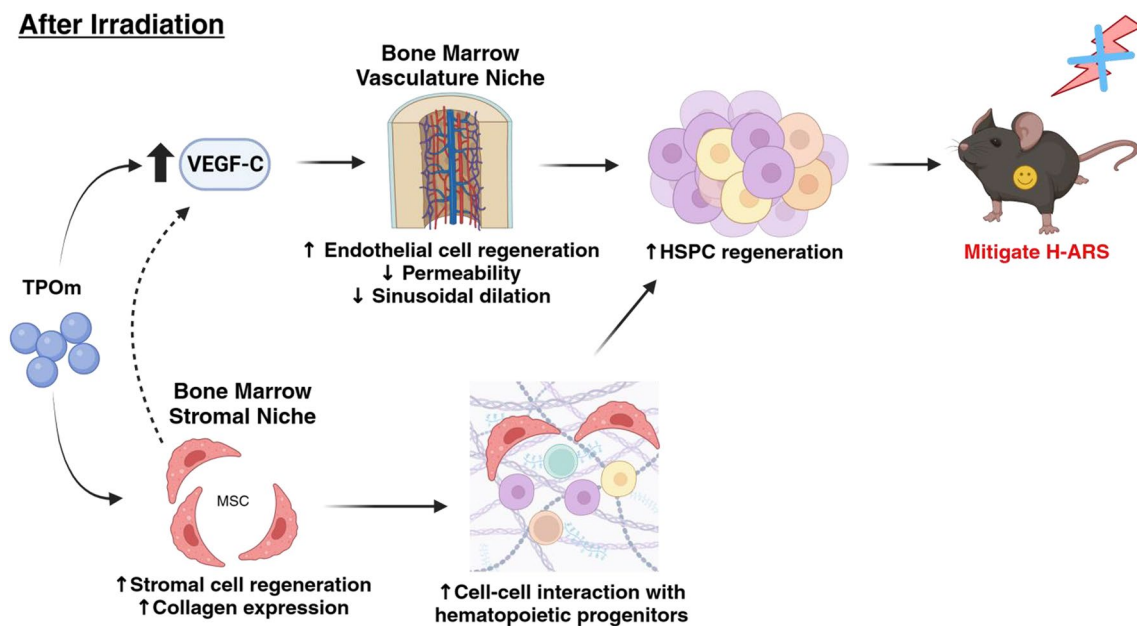


**Fig. 7** Summary of TPOm's effect on BM vascular and stromal niches for HSPC regeneration after irradiation to mitigate H-ARS

In conclusion, our study has unveiled novel functions of TPOm (JNJ-26366821) in regulating the vascular and stromal niches in the BM, fostering the regeneration of HSPCs in irradiated mice. TPOm's stimulation of VEGF secretion contributed to the maintenance vascular integrity in irradiated mice. Additionally, TPOm promoted

MSCs to interact with other progenitors in the BM. These TPOm-induced effects collectively resulted in a significant improvement in the survival of the TBI mice, a model of H-ARS (Fig. 7). Taken together, TPOm is positioned as a clinical ready drug, meriting further development as radiation MCM for potential FDA approval.

## Materials and methods

### Key resources table

Reagent or resource	Source	Identifier	
Antibodies			
Hematopoietic stem and progenitor cell analysis (used 1:100 dilution unless otherwise noted)	PerCP-Cyanine5.5 anti-mouse Lineage	BD Biosciences	Cat#561317; RRID:AB_10612020
	FITC anti-mouse Ly-6A/E (Sca-1, clone D7)	Biolegend	Cat# 108106, RRID:AB_313343
	Alexa Fluor 700 anti-mouse Ly-6A/E (Sca-1, clone D7)	Biolegend	Cat# 108142, RRID:AB_2565959
	APC anti-mouse CD117 (c-kit, clone 2B8)	Biolegend	Cat# 105811, RRID:AB_313220
	PE/Cyanine7 anti-mouse CD41 (clone MWRReg30; 1:200)	Biolegend	Cat# 133915, RRID:AB_11125173
	Alexa Fluor 700 anti-mouse CD34 (clone RAM34; 1:50)	BD Biosciences	Cat# 560518, RRID:AB_1727471
	Brilliant Violet 421 anti-mouse CD34 (clone SA376A4)	Biolegend	Cat# 152208, RRID:AB_2650766
	Pacific Blue anti-mouse CD150 (clone TC15-12F12.2)	Biolegend	Cat# 115924, RRID:AB_2270307
	Brilliant Violet 711 anti-mouse CD150 (clone TC15-12F12.2)	Biolegend	Cat# 115941, RRID:AB_2629660
	APC/Cyanine7 anti-mouse CD48 (clone HM48-1; 1:200)	Biolegend	Cat# 103431, RRID:AB_2561462
Brilliant Ultra-Violet 395 anti-mouse CD48 (clone HM48-1; 1:200)	BD Biosciences	Cat# 740236, RRID:AB_2739984	

Reagent or resource	Source	Identifier
Endothelial/ stromal cell analysis (used 1:100 dilution unless otherwise noted)	PerCP-Cyanine5.5 anti-mouse CD45 (clone 30-F11; 1:200)	Biologend Cat# 103132, RRID:AB_893340
	PerCP-Cyanine5.5 anti-mouse TER-119 (clone TER-119; 1:200)	Biologend Cat# 116228, RRID:AB_893636
	APC anti-mouse CD31 (clone 390)	Biologend Cat# 102409, RRID:AB_312904
	FITC anti-mouse CD31 (clone MEC13.3)	Biologend Cat# 102506, RRID:AB_312913
	Alexa Fluor 647 anti-mouse CD31 (clone MEC13.3)	Biologend Cat# 102516, RRID:AB_2161029
	Alexa Fluor 647 anti-mouse VE-Cadherin (clone BV13)	Biologend Cat# 138006, RRID:AB_10569114
	FITC anti-mouse CD62P (clone RB40.34)	BD Biosciences Cat# 553744, RRID:AB_395026
	Brilliant Violet 605 anti-mouse CD140a (clone APA5)	Biologend Cat# 135916, RRID:AB_2721548
	PE anti-mouse CD51 (clone RMV-7)	Biologend Cat# 104106, RRID:AB_2129493
	Unconjugated anti-mouse VEGF Receptor 2 (clone D5B1)	Cell Signaling Cat# 9698, RRID:AB_11178792
	Unconjugated anti-mouse VEGF Receptor 3	R&D Cat# AF743, RRID:AB_355563
	Unconjugated anti-mouse Leptin Receptor	R&D Cat# AF497, RRID:AB_2281270
	Biotinylated anti-mouse Leptin Receptor	R&D Cat# BAF497, RRID:AB_2296953
	Biotinylated anti-mouse CD202b (TIE2, clone TEK4)	Biologend Cat# 124006, RRID:AB_2203221
	AffiniPure F (ab) <sub>2</sub> Fragment Donkey Anti-Goat IgG (H + L) Alexa Fluor 594	Jackson ImmunoResearch Cat# 705-586-147, RRID:AB_2340434
AffiniPure F (ab) <sub>2</sub> Fragment Donkey Anti-Rabbit IgG (H + L) Alexa Fluor 647	Jackson ImmunoResearch Cat# 711-606-152, RRID:AB_2340625	
Chemicals, Peptides, and Recombinant Proteins		
Thrombopoiein mimetic (TPOm)	Janssen Pharmaceuticals N/A	
Dispase II, powder	Gibco Cat# 17105041	
Collagenase, Tyoe IV, powder	Gibco Cat# 17104019	
Hank's balanced salt solution (HBSS)	Gibco Cat# 24020117	
Paraformaldehyde	Electron Microscopy Sciences Cat# 15710	
10% Neutral buffered formalin	Fisher Cat# F8775	
1X ACK lysing buffer	Lonza Cat# 10-548E	
AngioSense750 EX	PerkinElmer Cat# NEV10011EX	
Decal™ Decalcifier	StatLab Cat# 1211-1	
Commercial Assays		
Pierce™ BCA Protein Assay Kit	Thermo Scientific Cat# 23225	
VEGF-A ELISA	R&D Cat# MMV00, RRID:AB_2847842	
VEGF-C ELISA	Novus Biologicals Cat# NBP2-78893, RRID:AB_3083672	
Chromium Next GEM Single Cell 3' GEM, Library & Gel Bead Kit v3.1, 4 rxns	10X Genomics Cat# 1000128	
Deposited Data		
Single-cell RNA-seq	This paper	PRJNA1086455

Reagent or resource	Source	Identifier
Experimental Models: Organisms/Strains		
<i>Mus musculus</i> : C57BL/6 J	Jackson Laboratories	Stock #000664
<i>Mus musculus</i> : B6.Cg-Tg ( <i>Tek-cre</i> )1Ywa/J	Jackson Laboratories	Stock #008863, RRID:IMSR_JAX:008863, PMID: 11161575
<i>Mus musculus</i> : B6.Cg-Gt ( <i>ROSA</i> )26Sor <sup>tm14</sup> ( <i>CAG-tdTomato</i> )Hze/J	Jackson Laboratories	Stock #007914, RRID:IMSR_JAX:007914, PMID: 20023653
Software and Algorithms		
GraphPad Prism	GraphPad	v10.1, RRID:SCR_002798
FlowJo	BD Biosciences	v10.1, RRID:SCR_008520
Living Image	Perkin Elmer	v4.3.1, RRID:SCR_014247
Volocity	Quorum Technologies	v6.5.1, RRID:SCR_002668
Slidebook	Intelligent Imaging Innovations	v6.0, RRID: SCR_014300
FIJI	ImageJ	v1.53c, RRID:SCR_002285
CaseViewer (SlideViewer)	3DHISTECH	v2.4.0.119028, RRID:SCR_024885
CellRanger	10X Genomics	v7.0.1, RRID:SCR_017344
R	<a href="http://www.r-project.org/">http://www.r-project.org/</a>	RRID:SCR_001905
CellChat	<a href="http://www.cellchat.org/">http://www.cellchat.org/</a>	v1.6.1, RRID:SCR_021946
Seurat	<a href="https://satijalab.org/seurat/">https://satijalab.org/seurat/</a>	v4.4.0, RRID:SCR_016341
MAST	<a href="https://rglab.github.io/MAST/">https://rglab.github.io/MAST/</a>	v1.26.0, RRID:SCR_016340
SCPA	<a href="https://jackbibby1.github.io/SCPA/">https://jackbibby1.github.io/SCPA/</a>	v1.5.4, RRID:SCR_024909

## Animals

C57BL/6J (wild-type; stock no. 000664), B6.Cg-Tg (*Tek-cre*)1Ywa/J (TIE2-cre; stock no. 008863), B6.Cg-Gt (*ROSA*)26Sor<sup>tm14</sup> (*CAG-tdTomato*)Hze/J (tdTomato; stock no. 007914) mice were purchased from Jackson Laboratories (Bar Harbor, ME). B6.Cg-Tg (*Tek-cre*)1Ywa/J and B6.Cg-Gt (*ROSA*)26Sor<sup>tm14</sup> (*CAG-tdTomato*)Hze/J were crossed together to generate constitutive Tek-cre; tdTomato (TIE2-tdTomato) mice in our facilities. All mice were acclimated for 1 week prior to experiments and group housed (no more than 5 per cage) in pathogen-free conditions under a 14:10 h light:dark cycle. Moreover, mice were housed at 20 °C to 22 °C with 30–70% humidity and fed ad libitum (Lab Diet 5001). To limit pathogen transmission, water was acidified to a pH of 2.5 to 3.0 with HCl for survival studies. All experiments were carried out using gender-matched littermate controls where appropriate. All mice in this study were used at 9–14 weeks of age. Both males and females were used for experiments.

## Preparation and injection of TPOM (JNJ-26366821)

TPOM was supplied as a powder for reconstitution at 1 mg/mL in sterile PBS. TPOM dosing formulations were stored protect from light, refrigerated (set to 2–8 °C) pending use for dosing within one day of preparation. Drug substance and stock solutions were stored protected from light in a –80 °C freezer. Stock solutions in

the concentration at 1 mg/mL can be stored in the above referenced freezer conditions for up to 8 weeks. Either TPOM or its vehicle were injected once subcutaneously at the nape, 24 h post-TBI. Based on a dose-escalation experiments of TPOM from a prior study, mice were dosed at 0.3 or 1.0 mg/kg [37].

## Irradiation

For <sup>137</sup>Cs TBI, mice were anesthetized with 60:9 mg/kg ketamine:xylazine, which was equivalent to about 100 μL/mouse, and placed in single chambers of a round brass animal holder for the Shepherd Mark I irradiator. Brass container was placed on a rotating plate to expose them to uniform total body γ-irradiation according to the manufacturer's specifications with a dose rate of about 1.90 Gy/min. TBI doses of 7.00 and 8.80/9.00 Gy were used for sublethal and lethal doses, respectively.

For X-ray total body irradiation, using a CIX-3 orthovoltage source (Xstrahl), unanesthetized mice were placed into a Plexiglas jig. The X-ray irradiator was operated at 300 kVp, 10 mA with either 1 mm Cu at a dose rate of 1.89 Gy/min or 4 mm Cu filtration (for scRNA-seq data) at a dose rate of 1.12 Gy/min at a 40 cm source surface distance. All irradiation was performed in the morning. Doses and dosimetry were determined as described in our previous publication comparing <sup>137</sup>Cs γ-radiation to orthovoltage X-rays [41].

### Complete blood count

At the time of euthanasia, mice were subjected to isoflurane overdose and blood was collected via cardiac puncture into K2EDTA coated microtainer tubes (BD Pharmingen, cat# 365967). Automated complete blood count with differential was performed using a Hemavet 950FS instrument (Drew Scientific).

### Bone marrow histology

Sternum was fixed in 10% neutral-buffered formalin (Fisher, cat# F8775) overnight at room temperature, followed by decalcification (StatLab, cat# 1211-1) overnight at room temperature. Sternum was then embedded in paraffin. Paraffin sections were cut at 5  $\mu$ m intervals and stained with hematoxylin and eosin (H&E). Slides were imaged on the P250 Slide Scanner (3DHISTEC) using the 20 $\times$  objective. Megakaryocytes were quantified manually using FIJI (ImageJ v1.53c). Adipocytes were quantified using QuPath [70] software with the MarrowQuant script as described previously [40].

### Flow cytometry and cell sorting

For analysis of hematopoietic cells, femurs were flushed with 2% FBS-PBS 2 mM EDTA (FPE) buffer with a 21G needle and for analysis of endothelial and stromal cells, tibias were flushed and digested with 1 mg/mL of collagenase IV (Gibco, cat# 17104019) and 2 mg/mL of dispase (Gibco, cat# 17105041) in Hank's balanced salt solution (HBSS) (Gibco, cat# 24020117) for a total of 30 min at 37  $^{\circ}$ C with an inversion at 15 min as previously described [12, 15]. After either procedure, cell pellet was resuspended in 1X ACK lysing buffer (Lonza, cat# 10-548E) to red blood cell lysis. The suspension was filtered through 70  $\mu$ m nylon mesh and counted using TC20 automated cell counter (BioRad) in 0.4% (w/v) Trypan Blue.

For FACS analysis, cells were incubated with Live/Dead Zombie NIR fixable dye (Biolegend, cat# 423106) in PBS/2 mM EDTA at room temperature for 15 min. After, primary antibodies were diluted in FPE buffer and incubated with cells for 30 min at 4  $^{\circ}$ C. The antibodies used for hematopoietic stem and progenitor cell analysis were diluted at 1:100 unless otherwise specified (see Key Resources Table): PerCP-Cyanine5.5 anti-mouse Lineage Cocktail, FITC anti-mouse Ly-6A/E (Sca-1), Alexa Fluor 700 anti-mouse Sca-1, APC anti-mouse CD117 (c-kit), PE/Cyanine7 anti-mouse CD41 (1:200 dilution), Alexa Fluor 700 anti-mouse CD34 (1:50 dilution), Brilliant Violet 421 anti-mouse CD34, Pacific Blue anti-mouse CD150, Brilliant Violet 711 anti-mouse CD150, APC/Cyanine7 anti-mouse CD48 (1:200 dilution), Brilliant Ultra-Violet 395 anti-mouse CD48 (1:200 dilution). The antibodies used for endothelial/stromal cell analysis

were diluted at 1:100 unless otherwise specified (see Key Resources Table): PerCP-Cyanine5.5 anti-mouse CD45 (1:200 dilution), PerCP-Cyanine5.5 anti-mouse TER-119 (1:200 dilution), APC anti-mouse CD31, FITC anti-mouse CD31, FITC anti-mouse CD62P, Brilliant Violet 605 anti-mouse CD140 $\alpha$ , PE anti-mouse CD51, anti-mouse VEGF Receptor 2, AffiniPure F (ab')<sub>2</sub> Fragment Donkey Anti-Rabbit IgG (H+L) Alexa Fluor 647 (1:300 dilution), anti-mouse Leptin Receptor, AffiniPure F (ab')<sub>2</sub> Fragment Donkey Anti-Goat IgG (H+L) Alexa Fluor 594 (1:300 dilution), Streptavidin Alexa Fluor 488 (1:300 dilution), anti-mouse TIE2, Streptavidin PE-Cy5 (1:300 dilution). Cells were washed with 2% FBS-PBS solution and incubated with secondary antibodies for 30 min, if necessary. Cells were resuspended in FPE buffer and acquired on Cytex Aurora with SpectroFlo software or BD LSRII with FACS Diva software on flow cytometer. Cell sorting was performed on FACS Aria Cell Sorter (BD Biosciences) as previously described [23]. Dead cells and debris were excluded by FSC, SSC, and Live/Dead staining. Data analysis was done through FlowJo (Tree Star, v10.1) software.

### Immunofluorescence imaging and analysis

In vivo staining of bone marrow endothelial cells was done via retroorbital perfusion of EC-specific antibodies Alexa Fluor 647 anti-mouse VE-Cadherin (5  $\mu$ g, Biolegend, cat# 138006, clone BV13) and Alexa Fluor 647 anti-mouse CD31 (5  $\mu$ g, Biolegend, cat# 102516, clone MEC13.3) for 15 min. Femoral bones were extracted and fixed overnight in 4% paraformaldehyde (PFA, Electron Microscopy Sciences, cat# 15710), incubated in 30% sucrose for at least 24 h and embedded in optical cutting temperature compound (OCT) (Fisher, cat# 4585). For whole-mount staining, bones were shaved on a cryostat until the bone marrow cavity was fully exposed. Bones were carefully harvested from melting OCT and stained in Eppendorf tubes with anti-mouse VEGFR3 (unconjugated, 5  $\mu$ g/femur, R&D, cat# AF743) and Hoechst 33342 for nuclei staining (1:2000 dilution, Thermo Scientific, cat# 62249) as previously described [22].

Similarly, for whole-mount preparation of sternum, sternums were collected and bisected sagittally for exposure of the bone marrow cavity then fixed in 4% PFA for 30 min, washed 3X with PBS, then stained with FITC anti-mouse Ly-6A/E [Sca-1; (1:100 dilution, Biolegend, cat# 108106, clone D7)] and Hoechst 33342 for nuclei staining as previously described [7]. Images were acquired using a water immersion lens on the ZEISS AXIO examiner D1 microscope (Zeiss) with a confocal scanner unit, CSUX1CU (Yokogawa), and reconstructed in three dimensions with Slide Book software (Intelligent Imaging Innovations, v6.0) or analyzed using Volocity

software (Quorum Technologies, v6.5.1). Briefly, original images were loaded into Volocity as TIFF file formats. Brightness-contrast and noise reduction modifications were applied to each channel for the whole image. Quantification of vessel area and quantification of Sca-1<sup>+</sup> cells were performed in Volocity.

#### ELISA

Plasma was collected after complete blood count analysis using 8000×g for 5 min to spin down whole blood and stored at -80 °C. Bone marrow supernatant was collected by flushing a 200 µL of 1X PBS through two femurs. The solution was centrifuged at 300×g for 5 min to separate cells and supernatant was separately stored at -80 °C. Protein concentrations for the BM supernatant was determined using BCA Protein Assay kit (Thermo Scientific, cat# 23,225) according to manufacturer's instructions with BSA as a standard. ELISA for VEGF-A (R&D, cat# MMV00) and VEGF-C (Novus Biologicals, cat# NBP2-78893) were performed according to manufacturer's instructions. Standard dilutions for plasma and 10 µg of total protein for BM supernatant were loaded for either ELISA for standardization.

#### In vivo imaging

IVIS was performed on the Caliper Life Sciences IVIS Spectrum system. Mice were intravenously perfused with AngioSense750 EX (PerkinElmer, cat# NEV10011EX) on day 3 after irradiation as per manufacturer's instructions. On day 5 after irradiation, mice were anesthetized with isoflurane (2% v/v with oxygen as the carrier gas) in an inhalation chamber (VetEquip, cat# 911103) and maintained as mice were in the IVIS. The radiant efficiency, a relative measure of photon emission from the animal (photons/s/cm<sup>2</sup>), was measured in a standardized region of interest (ROI) with the variables of exposure time, binning, and focal length/stop also standardized. Fluorescence measurements were acquired with Living Image (Perkin Elmer, v4.3.1) and are expressed as a pseudocolor on a gray background, with red representing the lowest intensity and blue the highest.

#### Library preparation and sequencing

Single-cell RNA sequencing libraries involved sorted bone marrow cells stained with CD45, TER-119, and CD31 markers. These libraries were generated from a total of ~20,000 individual cells, combining cell-multiplexing oligos (CMOs) from one male and one female mouse, contributing about ~10,000 cells each. The process involved generating cDNA within individual cell-gel bead emulsion micro-reactors, during which barcodes were added at both cellular and molecular levels. This

barcoding allowed for the combination of the cDNA from individual cells for further library processing. Unique molecular barcodes (UMIs) were utilized to ensure that amplification artifacts did not distort the analysis. The prepared libraries underwent sequencing for 4000 M reads (PE150), with approximately 400 million read pairs for gene expression libraries and about 100 million read pairs for CMO libraries, all sequenced on an Illumina HiSeq 2500 system.

#### Single-cell RNA sequencing analysis

Data were analyzed with a high-throughput next-gen sequencing pipeline. Cell Ranger (7.0.1) was used for data preprocessing. Seurat package (4.4.0) was harnessed for data analysis. Cells filtering was performed with following thresholds: nFeature\_RNA > 200 & nFeature\_RNA < 6000 & percent.mt < 5. Cells were identified based on their Seurat clustering and their positive markers as well as using specific markers expressions available from literature. Cell communications scores were calculated and visualized using CellChat package (1.6.1). Differential expression was calculated using MAST package (1.26.0) that allowed for adjustment to confounding variables (Sex, nCount\_RNA, percent.mt, S.Score). Pathway analysis was performed with SCPA package (1.5.4) with MSigDB Mus musculus C5.BP pathway library.

#### Statistical analysis

Statistical analysis and graphs were conducted and generated through GraphPad Prism (v10.1). Specific statistical details for each figure can be found at the end of each figure legend. Survival was analyzed using Kaplan–Meier curves with log-rank Mantel–Cox test. One-way ANOVA was used to compare three or more groups with a single control group using post hoc Dunnett test for multiple comparisons correction. Multiple Student's *t* tests were performed for statistical analysis between vehicle and TPOM-treated with post hoc Holm–Sidak test for multiple comparisons. Outliers were determined using ROUT with a Q=0.2% and excluded only in irradiated flow cytometry experiments (Fig. 2 and Additional file 1: Fig. S2). Naïve controls were excluded from statistical analysis and only shown as reference. No statistical method was used to determine sample size. All mice from experiments were randomized for each experimental group and investigators were not blinded to their allocation. *n* represent the number of mice used in each experiment which was replicated 2–4 times. Results were considered statistically significant when *p* < 0.05 and \**p* < 0.05, \*\**p* < 0.01, \*\*\**p* < 0.001, \*\*\*\**p* < 0.0001. All data are shown as mean ± SEM.

## Abbreviations

TBI	Total body irradiation
BM	Bone marrow
H-ARS	Hematopoietic acute radiation syndrome
TPOm	Thrombopoietin mimetic, JNJ-26366821
HSPC	Hematopoietic stem and progenitor cell
MSC	Mesenchymal stromal cell
MCM	Medical countermeasure
LSK	Lineage <sup>-</sup> , Sca-1 <sup>+</sup> , c-kit <sup>+</sup>
LT-HSC	Long-term hematopoietic stem cell
ST-HSC	Short-term hematopoietic stem cell
MPC	Myeloid progenitor cell
EPC	Endothelial progenitor cell
EC	Endothelial cell
AEC	Arteriolar endothelial cell
SEC	Sinusoidal endothelial cell
SCF	Stem cell factor
TNC	Triple negative cell; CD45 <sup>-</sup> , TER-119 <sup>-</sup> , CD31 <sup>-</sup>
VEGF	Vascular endothelial growth factor
TPO	Thrombopoietin
rhTPO	Recombinant human thrombopoietin
PLT	Platelets
WBC	White blood cells
NE	Neutrophils
LY	Lymphocytes
MKP	Megakaryocyte progenitor
sc	Subcutaneous
LD <sub>50</sub> DEATH/TIME	Lethal dose
VEGFR	Vascular endothelial growth factor receptor
MK_Prog	Megakaryocyte progenitor in single-cell data
Neutro_Prog	Neutrophil progenitor in single-cell data
Eo-Baso_Prog	Eosinophil-Basophil progenitor in single-cell data
Erythro_Prog	Erythroid progenitor in single-cell data
SCPA	Single cell pathway analysis
GOBP	Gene ontology biological pathways

## Supplementary Information

The online version contains supplementary material available at <https://doi.org/10.1186/s13287-024-03734-z>.

**Additional file 1: Figure S1.** TPOm augments the frequency of hematopoietic stem and progenitor, endothelial, and stromal cells in murine bone marrow at homeostasis. **(A)** Gating strategy and representative flow plots for identifying various hematopoietic stem cell populations for naïve and day 3 after TPOm treatment groups. **(B)** The frequency of live MPC, Mkp, LSK, ST-, and LT-HSC of naïve and TPOm-treated mice (n=3-4/group) over time. **(C)** Gating strategy and representative flow plots for identifying various endothelial cell and stromal populations for naïve and day 3 after TPOm treatment groups. **(D)** The frequency of live EC, EPC, AEC, SEC, and MSC of naïve and TPOm-treated mice (n=3-4/group) over time. Data are expressed as mean ± SEM. \**p* < 0.05 vs. naïve assessed by one-way ANOVA with post hoc Dunnett test for multiple comparisons. **Figure S2.** TPOm increases the frequency of hematopoietic stem and progenitor, endothelial, and stromal cells in murine bone marrow following 7.0 Gy sublethal total body irradiation. **(A)** The frequency of live MPC, Mkp, LSK, ST-, and LT-HSC of naïve and TPOm-treated mice (n=4-29/group) over time. **(B)** The frequency of live EC, EPC, AEC, SEC, and MSC of naïve and TPOm-treated mice (n=4-29/group) over time. Data are expressed as mean ± SEM. \**p* < 0.05, \*\**p* < 0.01, \*\*\**p* < 0.001 vehicle vs. TPOm-treated assessed by unpaired Student's *t*-test with post hoc Holm-Sidak method for multiple comparisons. Outliers were determined using ROUT with a *Q* = 0.2%. **Figure S3.** TPOm increases survival of female mice and reduces hemorrhaging in the bone marrow of male mice after lethal total body irradiation. **(A)** Kaplan-Meier survival curve of vehicle and TPOm treated female mice for 30 days after 7.2 Gy X-ray TBI. **(B)** The percentage of body weight change over 30 days after 7.2 Gy X-ray TBI in female mice. **(C)** Representative H&E images of sternal bone marrow from 8.8 Gy (<sup>137</sup>Cs) irradiated vehicle and TPOm-treated mice on days 7 and 14 after irradiation. For survival the Log-rank (Mantel-Cox) test was used for curve comparison. Light blue

arrow, adipocytes; dark blue box, hemorrhaging. Scale bar is 100 μm. For the percent weight change data are expressed as mean ± SEM. **Figure S4.** TPOm promotes secretion of VEGF-A and VEGF-C in healthy mice. **(A, B)** ELISA of VEGF-A in **(A)** serum and in **(B)** BM after TPOm treatment. **(C, D)** ELISA of VEGF-C in **(C)** serum and in **(D)** BM after TPOm treatment. Data are expressed as mean ± SEM. \**p* < 0.05 vs. naïve assessed by one-way ANOVA with post hoc Dunnett test for multiple comparisons. **Figure S5.** TPOm increases *Mki67* expression on megakaryocyte progenitors. **(A)** Cell cycle status of individual UMAP per treatment group. **(B)** Violin plots of the expression level of *Mki67* on megakaryocyte progenitors for each treatment group. **Figure S6.** MSCs express various collagens and VEGFs. **(A)** Dot plot of genes highly specific to the MSC cluster of the TNC in the BM. **(B)** Expression levels of different collagens and their interacting partners on each cluster. **(C)** Expression levels of different vascular growth factors secreted by each cluster.

## Acknowledgements

We are incredibly grateful to the laboratory of Dr. Paul Frenette for teaching us bone marrow flow cytometry and imaging techniques. We thank the Albert Einstein Cancer Center for their support (P30CA013330). We also thank the Albert Einstein College of Medicine Histology and Comparative Pathology Facility, Mr. David Reynolds of the Genomics Core Facility and Singulomics for their expertise in sequencing. In Vivo Imaging System Facility (S10RR027308-01), Flow Cytometry Core Facility (S10OD026833-01) and Analytical Imaging Facility (S10OD019961-01) for their valuable aid with this project. Lastly, we would like to thank Dr. Merrilline Satyamitra for her intellectual input in our scientific discussions.

## Author contributions

Conceptualization, J.V., S.K., G.E., and C.G.; Methodology, J.V., B.M., S.K., K.S., P.S.F. and W.Y.; Investigation, J.V., B.M., S.K., B.I.B., S.S., K.S., and W.Y.; Formal Analysis, J.V. and B.M.; Writing—Original Draft, J.V. and W.Y.; Writing—Review and Editing; J.V., B.M., S.K., B.I.B., G.E., A.V., S.P.G., W.Y., and C.G.; Visualization, J.V., B.M., and W.Y.; Resources, G.E., P.S.F., and C.G.; Funding Acquisition, C.G.; Supervision, S.K., W.Y., and C.G. All authors read and approved the final manuscript. S.K. contributed to this article in their personal capacity prior to joining the National Institutes of Health. The views expressed are their own and do not necessarily represent the views of the National Institutes of Health or the United States Government.

## Funding

This work was funded by NIAID U01A1133608.

## Availability of data and materials

The datasets supporting the conclusions of this article are available in the Figshare repository, with the following link: <https://figshare.com/s/79412a5256d7cd59b306>. Single-cell RNA sequencing data are deposited under BioProject number PRJNA1086455. This paper does not report original code. All code used in this publication are publicly available online. Further information and requests for resources and reagents should be directed to and will be fulfilled upon reasonable request by the corresponding author, Dr. Chandan Guha (cguhamd@gmail.com).

## Declarations

### Ethics approval and consent to participate

The animal study protocol used for this study is entitled "Develop mitigation strategies for radiation induced vascular injuries," and was under protocol number 00001992 which was initially approved on November 11, 2019. All animal experiments and procedures were performed in accordance with protocols approved from the Institutional Animal Care and Use Committee at the Albert Einstein College of Medicine. Animal care and all experimental procedures were conducted in accordance with the Animal Research: Reporting of In Vivo Experiments (ARRIVE) 2.0 guidelines.

### Competing interests

G.E. was an employee of Janssen Pharmaceuticals and worked on the development of thrombopoietin mimetic (JNJ-26366821). J.V., W.Y., G.E., and C.G.

have patented TPOm under US20230104658A1. G.E. and C.G. are co-founders of Bio Convergent Health. All other authors declare no competing interests.

#### Author details

<sup>1</sup>Department of Radiation Oncology, Albert Einstein College of Medicine, 1300 Morris Park Avenue, Bronx, NY 10461, USA. <sup>2</sup>Department of Pathology, Albert Einstein College of Medicine, Bronx, NY, USA. <sup>3</sup>Department of Molecular Pharmacology, Albert Einstein College of Medicine, Bronx, NY, USA. <sup>4</sup>Johnson & Johnson, Office of the Chief Medical Officer, New Brunswick, NJ, USA. <sup>5</sup>Department of Developmental and Molecular Biology, Albert Einstein College of Medicine, Bronx, NY, USA. <sup>6</sup>Armed Forces Radiobiology Research Institute, Uniformed Services University of the Health Sciences, Bethesda, MD, USA. <sup>7</sup>Department of Cell Biology, Albert Einstein College of Medicine, Bronx, NY, USA. <sup>8</sup>Present Address: National Institute of Allergy and Infectious Diseases, National Institutes of Health, Rockville, MD, USA. <sup>9</sup>Present Address: Bioconvergent Health, LLC, Purchase, NY, USA.

Received: 9 February 2024 Accepted: 16 April 2024

Published online: 29 April 2024

#### References

- Dainiak N. Hematologic consequences of exposure to ionizing radiation. *Exp Hematol*. 2002;30(6):513–28.
- Singh VK, Seed TM. A review of radiation countermeasures focusing on injury-specific medicinals and regulatory approval status: part I. Radiation sub-syndromes, animal models and FDA-approved countermeasures. *Int J Radiat Biol*. 2017;93(9):851–69. <https://doi.org/10.1080/09553002.2017.1332438>.
- Comazzetto S, Shen B, Morrison SJ. Niches that regulate stem cells and hematopoiesis in adult bone marrow. *Dev Cell*. 2021;56(13):1848–60.
- Hoggatt J, Kfoury Y, Scadden DT. Hematopoietic stem cell niche in health and disease. *Annu Rev Pathol*. 2016;11:555–81.
- Mendez-Ferrer S, Michurina TV, Ferraro F, Mazloom AR, MacArthur BD, Lira SA, Scadden DT, Ma'ayan A, Enikolopov GN, Frenette PS. Mesenchymal and haematopoietic stem cells form a unique bone marrow niche. *Nature*. 2010;466(7308):829–34.
- Kiel MJ, Yilmaz OH, Iwashita T, Yilmaz OH, Terhorst C, Morrison SJ. SLAM family receptors distinguish hematopoietic stem and progenitor cells and reveal endothelial niches for stem cells. *Cell*. 2005;121(7):1109–21.
- Asada N, Kunisaki Y, Pierce H, Wang Z, Fernandez NF, Birbrair A, Ma'ayan A, Frenette PS. Differential cytokine contributions of perivascular haematopoietic stem cell niches. *Nat Cell Biol*. 2017;19(3):214–23.
- Mendelson A, Frenette PS. Hematopoietic stem cell niche maintenance during homeostasis and regeneration. *Nat Med*. 2014;20(8):833–46.
- Chen Q, Liu Y, Jeong HW, Stehling M, Dinh VV, Zhou B, Adams RH. Ape-1(+/-) endothelial niche cells control hematopoiesis and mediate vascular regeneration after myeloablative injury. *Cell Stem Cell*. 2019;25(6):768–83.
- Comazzetto S, Murphy MM, Berto S, Jeffery E, Zhao Z, Morrison SJ. Restricted hematopoietic progenitors and erythropoiesis require SCF from leptin receptor+ niche cells in the bone marrow. *Cell Stem Cell*. 2019;24(3):477–86.
- Ding L, Saunders TL, Enikolopov G, Morrison SJ. Endothelial and perivascular cells maintain haematopoietic stem cells. *Nature*. 2012;481(7382):457–62.
- Kunisaki Y, Bruns I, Scheiermann C, Ahmed J, Pinho S, Zhang D, Mizoguchi T, Wei Q, Lucas D, Ito K, et al. Arteriolar niches maintain haematopoietic stem cell quiescence. *Nature*. 2013;502(7473):637–43.
- Itkin T, Gur-Cohen S, Spencer JA, Schajnovitz A, Ramasamy SK, Kusumbe AP, Ledergor G, Jung Y, Milo I, Poulos MG, et al. Distinct bone marrow blood vessels differentially regulate haematopoiesis. *Nature*. 2016;532(7599):323–8.
- Zhou BO, Ding L, Morrison SJ. Hematopoietic stem and progenitor cells regulate the regeneration of their niche by secreting Angiopoietin-1. *Elife*. 2015;4:e05521.
- Xu C, Gao X, Wei Q, Nakahara F, Zimmerman SE, Mar J, Frenette PS. Stem cell factor is selectively secreted by arterial endothelial cells in bone marrow. *Nat Commun*. 2018;9(1):2449.
- Greenbaum A, Hsu YM, Day RB, Schuettelpelz LG, Christopher MJ, Borgerding JN, Nagasawa T, Link DC. CXCL12 in early mesenchymal progenitors is required for haematopoietic stem-cell maintenance. *Nature*. 2013;495(7440):227–30.
- Pinho S, Frenette PS. Hematopoietic stem cell activity and interactions with the niche. *Nat Rev Mol Cell Biol*. 2019;20(5):303–20.
- Yang J, Li M, Kamei N, Alev C, Kwon SM, Kawamoto A, Akimaru H, Masuda H, Sawa Y, Asahara T. CD34+ cells represent highly functional endothelial progenitor cells in murine bone marrow. *PLoS ONE*. 2011;6(5):e20219.
- Himburg HA, Sasine J, Yan X, Kan J, Dressman H, Chute JP. A molecular profile of the endothelial cell response to ionizing radiation. *Radiat Res*. 2016;186(2):141–52.
- Doan PL, Russell JL, Himburg HA, Helms K, Harris JR, Lucas J, Holshausen KC, Meadows SK, Daher P, Jeffords LB, et al. Tie2(+) bone marrow endothelial cells regulate hematopoietic stem cell regeneration following radiation injury. *Stem Cells*. 2013;31(2):327–37.
- Hooper AT, Butler JM, Nolan DJ, Kranz A, Iida K, Kobayashi M, Kopp HG, Shido K, Petit I, Yanger K, et al. Engraftment and reconstitution of hematopoiesis is dependent on VEGFR2-mediated regeneration of sinusoidal endothelial cells. *Cell Stem Cell*. 2009;4(3):263–74.
- Acar M, Kocherlakota KS, Murphy MM, Peyer JG, Oguro H, Inra CN, Jaiyeola C, Zhao Z, Luby-Phelps K, Morrison SJ. Deep imaging of bone marrow shows non-dividing stem cells are mainly perisinusoidal. *Nature*. 2015;526(7571):126–30.
- Boulais PE, Mizoguchi T, Zimmerman S, Nakahara F, Vivie J, Mar JC, van Oudenaarden A, Frenette PS. The majority of CD45(-) Ter119(-) CD31(-) bone marrow cell fraction is of hematopoietic origin and contains erythroid and lymphoid progenitors. *Immunity*. 2018;49(4):627–39.
- Fang S, Chen S, Nurmi H, Leppanen VM, Jeltsch M, Scadden D, Silberstein L, Mikkola H, Alitalo K. VEGF-C protects the integrity of the bone marrow perivascular niche in mice. *Blood*. 2020;136(16):1871–83.
- Kirito K, Fox N, Komatsu N, Kaushansky K. Thrombopoietin enhances expression of vascular endothelial growth factor (VEGF) in primitive hematopoietic cells through induction of HIF-1alpha. *Blood*. 2005;105(11):4258–63.
- Yagi M, Ritchie KA, Sitnicka E, Storey C, Roth GJ, Bartelmez S. Sustained ex vivo expansion of hematopoietic stem cells mediated by thrombopoietin. *Proc Natl Acad Sci U S A*. 1999;96(14):8126–31.
- Sitnicka E, Lin N, Priestley GV, Fox N, Brody VC, Wolf NS, Kaushansky K. The effect of thrombopoietin on the proliferation and differentiation of murine hematopoietic stem cells. *Blood*. 1996;87(12):4998–5005.
- Tong W, Ibarra YM, Lodish HF. Signals emanating from the membrane proximal region of the thrombopoietin receptor (mpl) support hematopoietic stem cell self-renewal. *Exp Hematol*. 2007;35(9):1447–55.
- Kaushansky K, Lok S, Holly RD, Brody VC, Lin N, Bailey MC, Forstrom JW, Buddle MM, Oort PJ, Hagen FS, et al. Promotion of megakaryocyte progenitor expansion and differentiation by the c-Mpl ligand thrombopoietin. *Nature*. 1994;369(6481):568–71.
- de Sauvage FJ, Hass PE, Spencer SD, Malloy BE, Gurney AL, Spencer SA, Darbonne WC, Henzel WJ, Wong SC, Kuang WJ, et al. Stimulation of megakaryocytopoiesis and thrombopoiesis by the c-Mpl ligand. *Nature*. 1994;369(6481):533–8.
- Li J, Yang C, Xia Y, Bertino A, Gaspy J, Roberts M, Kuter DJ. Thrombocytopenia caused by the development of antibodies to thrombopoietin. *Blood*. 2001;98(12):3241–8.
- Ikeda Y, Miyakawa Y. Development of thrombopoietin receptor agonists for clinical use. *J Thromb Haemost*. 2009;7(Suppl 1):239–44.
- Knight E, Eichenbaum G, Hillsamer V, Greway T, Tonelli A, Han-Hsu H, Zak-szewski C, Yurkow E, Shukla U, End D, et al. Nonclinical safety assessment of a synthetic peptide thrombopoietin agonist: effects on platelets, bone homeostasis, and immunogenicity and the implications for clinical safety monitoring of adverse bone effects. *Int J Toxicol*. 2011;30(4):385–404.
- Samtani MN, Perez-Ruixo JJ, Brown KH, Cerneus D, Molloy CJ. Pharmacokinetic and pharmacodynamic modeling of pegylated thrombopoietin mimetic peptide (PEG-TPOm) after single intravenous dose administration in healthy subjects. *J Clin Pharmacol*. 2009;49(3):336–50.
- de Laval B, Pawlikowska P, Barbieri D, Besnard-Guerin C, Cico A, Kumar R, Gaudry M, Baud V, Porteu F. Thrombopoietin promotes NHEJ DNA repair in hematopoietic stem cells through specific activation of Erk and NF-kappaB pathways and their target, IEX-1. *Blood*. 2014;123(4):509–19.
- de Laval B, Pawlikowska P, Petit-Cocault L, Bilhou-Nabera C, Aubin-Houzelstein G, Souyri M, Pouzoulet F, Gaudry M, Porteu F. Thrombopoietin-increased DNA-PK-dependent DNA repair limits hematopoietic stem and

- progenitor cell mutagenesis in response to DNA damage. *Cell Stem Cell*. 2013;12(1):37–48.
37. Kumar VP, Holmes-Hampton GP, Biswas S, Stone S, Sharma NK, Hritzo B, Guilfoyle M, Eichbaum G, Guha C, Ghosh SP. Mitigation of total body irradiation-induced mortality and hematopoietic injury of mice by a thrombopoietin mimetic (JNJ-26366821). *Sci Rep*. 2022;12(1):3485.
  38. Yamaguchi M, Hirouchi T, Yokoyama K, Nishiyama A, Murakami S, Kashiwakura I. The thrombopoietin mimetic romiplostim leads to the complete rescue of mice exposed to lethal ionizing radiation. *Sci Rep*. 2018;8(1):10659.
  39. Satyamitra M, Lombardini E, Graves J 3rd, Mullaney C, Ney P, Hunter J, Johnson K, Tamburini P, Wang Y, Springhorn JP, et al. A TPO receptor agonist, ALXN4100TPO, mitigates radiation-induced lethality and stimulates hematopoiesis in CD2F1 mice. *Radiat Res*. 2011;175(6):746–58.
  40. Tratwal J, Bekri D, Boussema C, Sarkis R, Kunz N, Koliqi T, Rojas-Sutterlin S, Schyrr F, Tavakol DN, Campos V, et al. MarrowQuant across aging and aplasia: a digital pathology workflow for quantification of bone marrow compartments in histological sections. *Front Endocrinol (Lausanne)*. 2020;11:480.
  41. Bell BI, Vercellino J, Brodin NP, Velten C, Nanduri LSY, Nagesh PKB, Tanaka KE, Fang Y, Wang Y, Macedo R, et al. Orthovoltage X-rays exhibit increased efficacy compared with gamma-rays in preclinical irradiation. *Cancer Res*. 2022;82(15):2678–91.
  42. Anghelina M, Moldovan L, Moldovan NI. Preferential activity of Tie2 promoter in arteriolar endothelium. *J Cell Mol Med*. 2005;9(1):113–21.
  43. Katoh O, Tsuchi H, Kawaiishi K, Kimura A, Satow Y. Expression of the vascular endothelial growth factor (VEGF) receptor gene, KDR, in hematopoietic cells and inhibitory effect of VEGF on apoptotic cell death caused by ionizing radiation. *Cancer Res*. 1995;55(23):5687–92.
  44. Zhou BO, Yu H, Yue R, Zhao Z, Rios JJ, Naveiras O, Morrison SJ. Bone marrow adipocytes promote the regeneration of stem cells and haematopoiesis by secreting SCF. *Nat Cell Biol*. 2017;19(8):891–903.
  45. Morikawa S, Mabuchi Y, Kubota Y, Nagai Y, Niibe K, Hiratsu E, Suzuki S, Miyauchi-Hara C, Nagoshi N, Sunabori T, et al. Prospective identification, isolation, and systemic transplantation of multipotent mesenchymal stem cells in murine bone marrow. *J Exp Med*. 2009;206(11):2483–96.
  46. Jin S, Guerrero-Juarez CF, Zhang L, Chang I, Ramos R, Kuan CH, Myung P, Plikus MV, Nie Q. Inference and analysis of cell-cell communication using Cell Chat. *Nat Commun*. 2021;12(1):1088.
  47. Hall EJG, Amato J. Radiobiology for the radiologist. In: *Radiobiology for the radiologist*. 8th Ed. edn. Two Commerce Square, 2001 Market Street, Philadelphia, PA 19103 USA: Lippincott Williams & Wilkins; 2019: 111–125.
  48. Singh V, Fatanmi O, Santiago P, Simas M, Hanlon B, Garcia M, Wise S. Current status of radiation countermeasures for acute radiation syndrome under advanced development. *J Radiat Cancer Res*. 2018;9(1):13–27.
  49. Shakyawar SK, Mishra NK, Vellichirammal NN, Cary L, Helikar T, Powers R, Oberley-Deegan RE, Berkowitz DB, Bayles KW, Singh VK, et al. A review of radiation-induced alterations of multi-omic profiles, radiation injury biomarkers, and countermeasures. *Radiat Res*. 2023;199(1):89–111.
  50. Micewicz ED, Damoiseaux RD, Deng G, Gomez A, Iwamoto KS, Jung ME, Nguyen C, Norris AJ, Ratikan JA, Ruchala P, et al. Classes of drugs that mitigate radiation syndromes. *Front Pharmacol*. 2021;12:666776.
  51. Cwirla SE, Balasubramanian P, Duffin DJ, Wagstrom CR, Gates CM, Singer SC, Davis AM, Tansik RL, Mattheakis LC, Boytos CM. Peptide agonist of the thrombopoietin receptor as potent as the natural cytokine. *Science*. 1997;276(5319):1696–9.
  52. Yoshihara H, Arai F, Hosokawa K, Hagiwara T, Takubo K, Nakamura Y, Gomei Y, Iwasaki H, Matsuoka S, Miyamoto K, et al. Thrombopoietin/MPL signaling regulates hematopoietic stem cell quiescence and interaction with the osteoblastic niche. *Cell Stem Cell*. 2007;1(6):685–97.
  53. Brizzi MF, Battaglia E, Montrucchio G, Dentelli P, Del Sorbo L, Garbarino G, Pegoraro L, Camussi G. Thrombopoietin stimulates endothelial cell motility and neoangiogenesis by a platelet-activating factor-dependent mechanism. *Circ Res*. 1999;84(7):785–96.
  54. Cardier JE, Dempsey J. Thrombopoietin and its receptor, c-mpl, are constitutively expressed by mouse liver endothelial cells: evidence of thrombopoietin as a growth factor for liver endothelial cells. *Blood*. 1998;91(3):923–9.
  55. Meijome TE, Ekwealor JTB, Hooker RA, Cheng YH, Ciovacco WA, Balamohan SM, Srinivasan TL, Chitteti BR, Eleniste PP, Horowitz MC, et al. C-Mpl is expressed on osteoblasts and osteoclasts and is important in regulating skeletal homeostasis. *J Cell Biochem*. 2016;117(4):959–69.
  56. Gao L, Decker M, Chen H, Ding L. Thrombopoietin from hepatocytes promotes hematopoietic stem cell regeneration after myeloablation. *Elife*. 2021;10:e69894.
  57. Decker M, Leslie J, Liu Q, Ding L. Hepatic thrombopoietin is required for bone marrow hematopoietic stem cell maintenance. *Science*. 2018;360(6384):106–10.
  58. Xing S, Shen X, Yang JK, Wang XR, Ou HL, Zhang XW, Xiong GL, Shan YJ, Cong YW, Luo QL, et al. Single-dose administration of recombinant human thrombopoietin mitigates total body irradiation-induced hematopoietic system injury in mice and nonhuman primates. *Int J Radiat Oncol Biol Phys*. 2020;108(5):1357–67.
  59. Bunin DI, Bakke J, Green CE, Javitz HS, Fielden M, Chang PY. Romiplostim (Nplate((R))) as an effective radiation countermeasure to improve survival and platelet recovery in mice. *Int J Radiat Biol*. 2020;96(1):145–54.
  60. Wong K, Chang PY, Fielden M, Downey AM, Bunin D, Bakke J, Gahagen J, Iyer L, Doshi S, Wierzbicki W, et al. Pharmacodynamics of romiplostim alone and in combination with pegfilgrastim on acute radiation-induced thrombocytopenia and neutropenia in non-human primates. *Int J Radiat Biol*. 2020;96(1):155–66.
  61. Kirito K, Kaushansky K. Thrombopoietin stimulates vascular endothelial cell growth factor (VEGF) production in hematopoietic stem cells. *Cell Cycle*. 2005;4(12):1729–31.
  62. Franiak-Pietryga I, Miyauchi S, Kim SS, Sanders PD, Sumner W, Zhang L, Mundt AJ, Califano JA, Sharabi AB. Activated B cells and plasma cells are resistant to radiation therapy. *Int J Radiat Oncol Biol Phys*. 2022;112(2):514–28.
  63. Singbrant S, Mattebo A, Sigvardsson M, Strid T, Flygare J. Prospective isolation of radiation induced erythroid stress progenitors reveals unique transcriptomic and epigenetic signatures enabling increased erythroid output. *Haematologica*. 2020;105(11):2561–71.
  64. Kaushansky K, Broudy VC, Grossmann A, Humes J, Lin N, Ren HP, Bailey MC, Papayannopoulou T, Forstrom JW, Sprugel KH. Thrombopoietin expands erythroid progenitors, increases red cell production, and enhances erythroid recovery after myelosuppressive therapy. *J Clin Invest*. 1995;96(3):1683–7.
  65. Tkachenko E, Rhodes JM, Simons M. Syndecans: new kids on the signalling block. *Circ Res*. 2005;96(5):488–500.
  66. Ponta H, Sherman L, Herrlich PA. CD44: from adhesion molecules to signalling regulators. *Nat Rev Mol Cell Biol*. 2003;4(1):33–45.
  67. Chen K, Liu J, Heck S, Chasis JA, An X, Mohandas N. Resolving the distinct stages in erythroid differentiation based on dynamic changes in membrane protein expression during erythropoiesis. *Proc Natl Acad Sci U S A*. 2009;106(41):17413–8.
  68. Yamashita Y, Oritani K, Miyoshi EK, Wall R, Bernfield M, Kincade PW. Syndecan-4 is expressed by B lineage lymphocytes and can transmit a signal for formation of dendritic processes. *J Immunol*. 1999;162(10):5940–8.
  69. Liem-Moolenaar M, Cerneus D, Mollouy CJ, End D, Brown KH, de Kam ML, Cohen AF, van Hensbergen Y, Burggraaf J. Pharmacodynamics and pharmacokinetics of the novel thrombopoietin mimetic peptide RWJ-800088 in humans. *Clin Pharmacol Ther*. 2008;84(4):481–7.
  70. Bankhead P, Loughrey MB, Fernandez JA, Dombrowski Y, McArt DG, Dunne PD, McQuaid S, Gray RT, Murray LJ, Coleman HG, et al. QuPath: Open source software for digital pathology image analysis. *Sci Rep*. 2017;7(1):16878.

## Publisher's Note

Springer Nature remains neutral with regard to jurisdictional claims in published maps and institutional affiliations.